Chemie der Erde 77 (2017) 207–224

Contents lists available at ScienceDirect

Chemie der Erde

journal homepage: www.elsevier.de/chemer

The Braunschweig meteorite – a recent L6 chondrite fall in Germany

Rainer Bartoschewitz[a,*], Peter Appel[b], Jean-Alix Barrat[c], Addi Bischoff[d], Marc W. Caffee[e], Ian A. Franchi[f], Zelimir Gabelica[g], Richard C. Greenwood[f], Mourad Harir[h,i], Dennis Harries[j], Rupert Hochleitner[k], Jens Hopp[l,m], Matthias Laubenstein[n], Barbara Mader[b], Rosa Marques[o], Andreas Morlok[d], Gert Nolze[p], Maria Isabel Prudêncio[o], Pierre Rochette[q], Alexander Ruf[h,i], Philippe Schmitt-Kopplin[h,i], Erhard Seemann[r], Marian Szurgot[s], Roald Tagle[t], Radosław A. Wach[u], Kees C. Welten[v], Mona Weyrauch[d,w], Karl Wimmer[x], The Braunschweig Meteorite Consortium

[a] *Bartoschewitz Meteorite Laboratory, Weiland 37, D-38518 Gifhorn, Germany*
[b] *Institut für Geowissenschaften, Universität Kiel, Ludewig-Meyn-Str. 10, D-24118 Kiel, Germany*
[c] *Université de Bretagne Occidentale, Institut Universitaire Européen de la Mer, Place Nicolas Copernic, F-29280 Plouzané Cedex, France*
[d] *Institut für Planetologie, Westfälische Wilhelms-Universität Münster, Wilhelm-Klemm Str. 10, D-48149 Münster, Germany*
[e] *PRIME Laboratory, Purdue University, West Lafayette, IN 47907, USA*
[f] *Planetary and Space Sciences, The Open University, Milton Keynes, MK7 6AA, United Kingdom*
[g] *Université de Haute Alsace, ENSCMu. Lab. GSEC, 3, Rue A. Werner, F-68093 Mulhouse Cedex, France*
[h] *Helmholtz-Zentrum, Muenchen, German Research Center for Environmental Health, Analytical BioGeoChemistry, Ingolstaedter Landstrasse 1, D-85764 Neuherberg, Germany*
[i] *Chair of Analytical Food Chemistry, Technische Universität München, D-85354 Freising-Weihenstephan, Germany*
[j] *Institut für Geowissenschaften, Friedrich-Schiller-Universität Jena, Carl-Zeiss-Promenade 10, D-07745 Jena, Germany*
[k] *Mineralogische Staatssammlung München (SNSB), Theresienstr. 41, D-80333 München, Germany*
[l] *Institut für Geowissenschaften, Im Neuenheimer Feld 234-236, D-69120 Heidelberg, Germany*
[m] *Klaus-Tschira-Labor für Kosmochemie, Im Neuenheimer Feld 234-236, D-69120 Heidelberg, Germany*
[n] *Lab. Naz. del Gran Sasso, Ist. Naz. di Fiscia Nucleare, Via G. Acitelli 22, I-67100 Assergi (AQ), Italy*
[o] *Centro de Ciências e Tecnologias Nucleares (C2TN), Instituto Superior Técnico, Universidade de Lisboa, EN 10 (km 139.7), 2695-066 Bobadela, Portugal*
[p] *Bundesanstalt für Materialforschung und –prüfung, Werkstofftechnik, Unter den Eichen 87, D-12205 Berlin, Germany*
[q] *CEREGE, BP80 13545, Aix en Provence, Cedex 4, France*
[r] *Steinaustrasse 5, D-38124 Braunschweig, Germany*
[s] *Center of Mathematics and Physics, Lodz University of Technology, Al. Politechniki 11, 90924 Lodz, Poland*
[t] *Bruker Nano GmbH, Schwarzschildstr. 12, D-12489 Berlin, Germany*
[u] *Institute of Applied Radiation Chemistry, Lodz University of Technology, Wróblewskiego 15, 93590 Lodz, Poland*
[v] *Space Sciences Laboratory, University of California, Berkeley, CA 94720, USA*
[w] *Institut für Mineralogie, Leibniz Universität Hannover, Callinstr. 3, D-30167 Hannover, Germany*
[x] *Rieskrater-Museum, Eugene-Shoemaker-Platz 1, D-86720 Nördlingen, Germany*

ARTICLE INFO

Article history:
Received 1 July 2016
Accepted 24 October 2016
Editorial handling - Klaus Keil

Keywords:
Braunschweig meteorite
L chondrite
Fall reconstruction
Petrology and mineralogy
Organic matter
IR spectroscopy
Bulk chemistry
Radionuclides
Noble gas isotopes
Specific heat

ABSTRACT

On April 23rd 2013 at 2:07 a.m., a 1.3 kg meteorite fell in the Braunschweig suburb Melverode (52° 13′ 32.19″ N. 10° 31′ 11.60″ E). Its estimated velocity was 250 km/h and it formed an impact pit in the concrete fall site with a diameter of 7 cm and a depth of 3 cm. Radial dust striae are present around the impact pit. As a result of the impact, the meteorite disintegrated into several hundred fragments with masses up to 214 g. The meteorite is a typical L6 chondrite, moderately shocked (S4) – but with a remarkably high porosity (up to 20 vol%). The meteorite was ejected from its parent body as an object with a radius of about 10–15 cm (15–50 kg). The U,Th-He gas retention age of ~550 Ma overlaps with the main impact event on the L-chondrite parent body ~470 Ma ago that is recorded by many shocked L chondrites. The preferred cosmic-ray exposure age derived from production of radionuclides and noble gas isotopes is (6.0 ± 1.3) Ma.

* Corresponding author.
E-mail address: Bartoschewitz.meteorite-lab@t-online.de (R. Bartoschewitz).

http://dx.doi.org/10.1016/j.chemer.2016.10.004
0009-2819/

1. Introduction

On the morning of April 23rd 2013, one of us (Erhard Seemann) came home and recognized a small unusual stone on the pebble concrete step at the front door of his house in Braunschweig-Melverode (52° 13′ 32.19″N, 10° 31′ 11.60″E). Looking around, he discovered a stone that fragmented into many small light gray fragments, surrounded by a gray corona of dust striae on the red brown concrete pavement (Fig. 1). He discovered additional fragments under his carport, on the driveway and on the road. In total, more than 100 pieces with masses ranging from <1 g up to 214 g, in total about 710 g, were discovered. In close proximity to the main mass of 214 g (Fig. 2), some red brown concrete fragments (up to 5 cm) were found that were ejected by the impact that formed a small crater of 7 cm width and 3 cm depth in the pavement. One of us (E. S.) documented his observations, collected the fragments and looked for scientific support. The Technische Universität Braunschweig informed Rainer Bartoschewitz about this possible meteorite fall, and on April 27th, R. B. inspected the fall site and confirmed the meteoritic origin of the fragments. An additional detailed search led to the discovery of more than 200 fragments between 84 g and <0.1 g totaling 540 g. The fragments were distributed up to 18 m from the impact point (Fig. S2), and traces of secondary impact were recognized at a nearby brick wall. A neighbor found another four fragments on his driveway on the morning of April 23rd, after he heard a sudden loud "whoosh" ending in a bang in the previous night around 2 a.m. In total ~1.3 kg of fragments were collected.

Efforts to canvas local residents resulted in only one reliable witness (Julian Mascow) from Ahlum near Wolfenbüttel (8 km from impact site). Outside he noticed a brightening of the southern sky for 1–2 s, which had a luminosity "like dawn". This brightening ended just above him – in the direction of Braunschweig – like a firecracker. Roughly 90 s later he heard a somewhat frightening explosion, followed by a rumbling noise that slowly abated.

The meteor-camera of Mark Vornhusen in Vechta (about 160 km from Braunschweig) documented the fireball (Fig. S3). Evaluation of geophysical data leads to following observations:

- The light meter of the weather station in Lindenberg/Brandenburg (approx. 240 km distance) recorded 5 s. of brightening (Fig. 2)
- The infra-sound station I26DE of the Bundesanstalt für Geowissenschaften und Rohstoffe near Haidmühle/Bavaria recorded a signal from a range of 231° ± 1° (corresponding to ± 14 km along the trajectory) (Fig. 3)

Several limited search attempts for additional meteorites were made in parts of the strewn field up to 5 km from the impact site without success. Systematic searches were not justified due to floods in the days following the fall, as well as heavy vegetation.

Fig. 1. Braunschweig meteorite impact site five hours after its fall. The meteorite shattered in hundreds of fragments while impact of about 250 km/h and destroyed the pavement (brick length 20 cm). The fragile 214 g meteorite main mass stick in the pavement "crater" of 7 cm width and 3 cm depth, surrounded by meteorite dust striae.

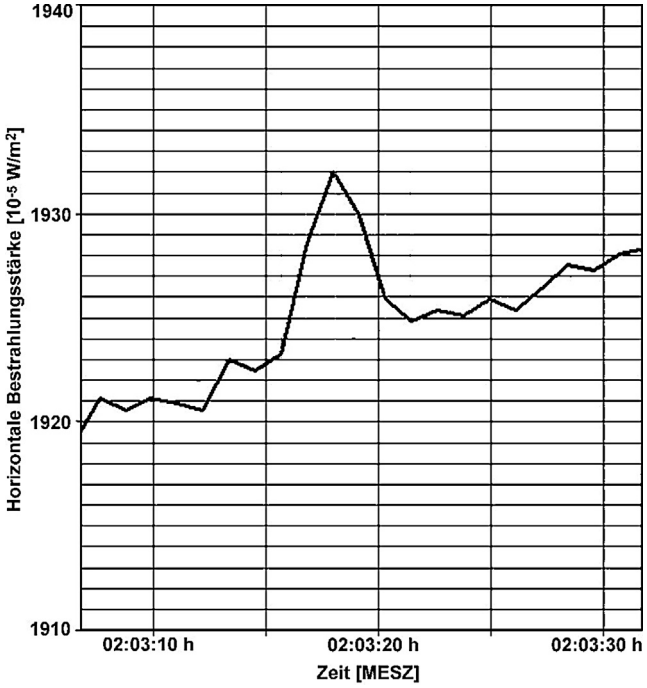

Fig. 2. Light meter signal of the weather station in Lindernberg/Brandenburg about 240 km from the fall area: duration 5 s with peak at 2:02:18 h.

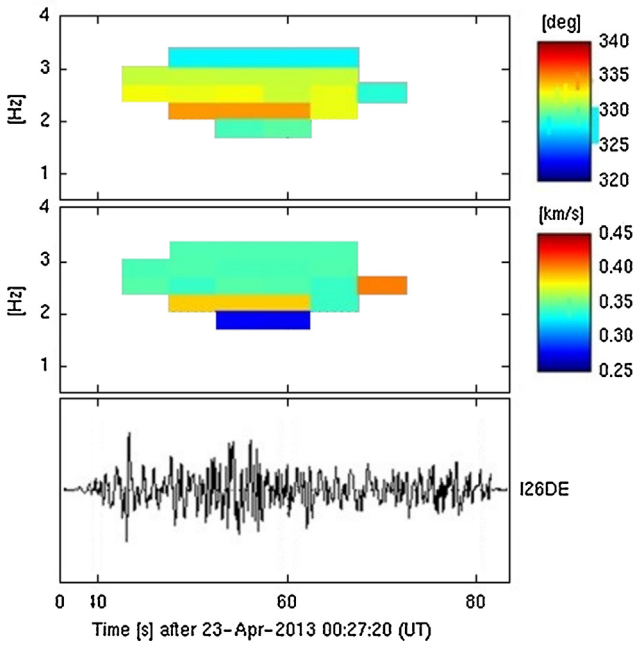

Fig. 3. Infra-sound record from station I26DE of Bundesanstalt für Geowissenschaften und Rohstoffe near Haidmühle/Bavaria: 331° ± 1° (corresponding to ±14 km along the trajectory).

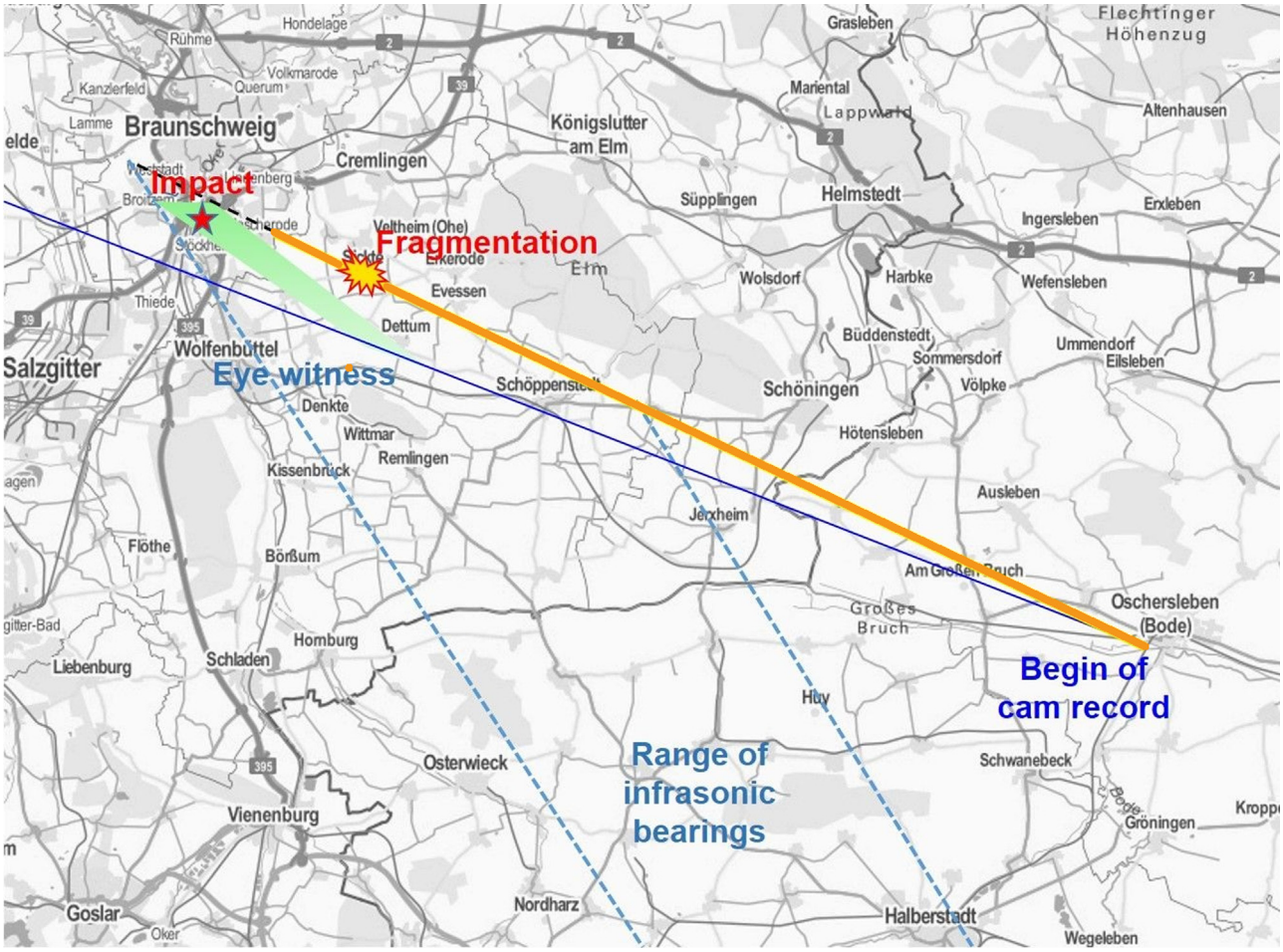

Fig. 4. Calculated meteorite strewn field (green) relative to luminous trajectory (yellow line), dark flight trajectory (black dashed line) and impact point (star). The blue line shows the start of cam record from Vechta and the area between the blue dashed lines reflects the range of infrasonic bearings. Background map: Landesamt für Geoinformation und Landesvermessung Niedersachsen (LGLN) GeoLife Navigator, www.geolife.de. (For interpretation of the references to colour in this figure legend, the reader is referred to the web version of this article.)

2. Fall reconstruction

Although the observational data for this fall are limited, they are sufficient to partially constrain the fall parameters. The photographic record from Vechta (Fig. 4) shows the upper part of the meteor at an azimuth of ~110° from North as an almost vertical line, defining a slightly inclined plane which contains the trajectory. The infrasonic record confines the event to the eastern part of that plane with respect to the impact point. Allowing for an initial height somewhere in between 75 km and 90 km, the trajectory azimuth can be narrowed down geometrically to an interval of two degrees around 296° in a first step.

To further constrain the fall scenario, the flight was simulated using the standard single-body algorithm (Ceplecha et al., 1998) with modifications to allow for at least one fragmentation. The necessary wind profile up to 30 km altitude was synthesized as an average, weighted according to distance, from data of the sounding stations Bergen (10238), Meiningen (10548), Lindenberg (10393) and Essen (10410) at 00UT. To land the 1.3 kg meteorite against the northern to western wind at the precisely known impact point we have to allow for a very low aerodynamic resistance. This is in accordance with the nose-cone shape of the fragment recovered from the crater. We infer that the final speed at impact was remarkably high at about 250 km/h. Reconciling all observations, including the 5 s illumination recorded by the light meter record, yields the parameters shown in Table 1. The specified ranges are estimated with 2 sigma uncertainty.

Table 1
Flight scenario of the Braunschweig meteoroid.

The specified ranges are estimated adopting a 2 sigma philosophy	
Initial mass at atmospheric entry (see also noble gas isotopes)	~50 kg
Velocity at atmospheric entry	20 ± 3 km/s
Initial height of luminous trajectory	81 ± 3 km
Trajectory azimuth	296° ± 0.5°
Trajectory slope	55° ± 7°
Length of luminous trajectory	82 ± 4 km
Fragmentation height	26 ± 2 km
Final height of luminous trajectory	16 ± 3 km
Dark flight duration	~120 s
Impact velocity	~70 m/s

The ablation was determined using the standard value for ordinary chondrites. This indicates an initial mass of roughly 50 kg, which is consistent with the radionuclide data, which set an upper limit for the meteoroid radius. The eye witness report suggests a minor fragmentation event at a high altitude somewhere around 26 km, high enough to allow for the development of the meteorite's aerodynamic shape during more than 1 s of oriented flight before the onset of dark flight. The strewn field is constrained to be a strip extending from the impact point towards the Southeast (Fig. 4).

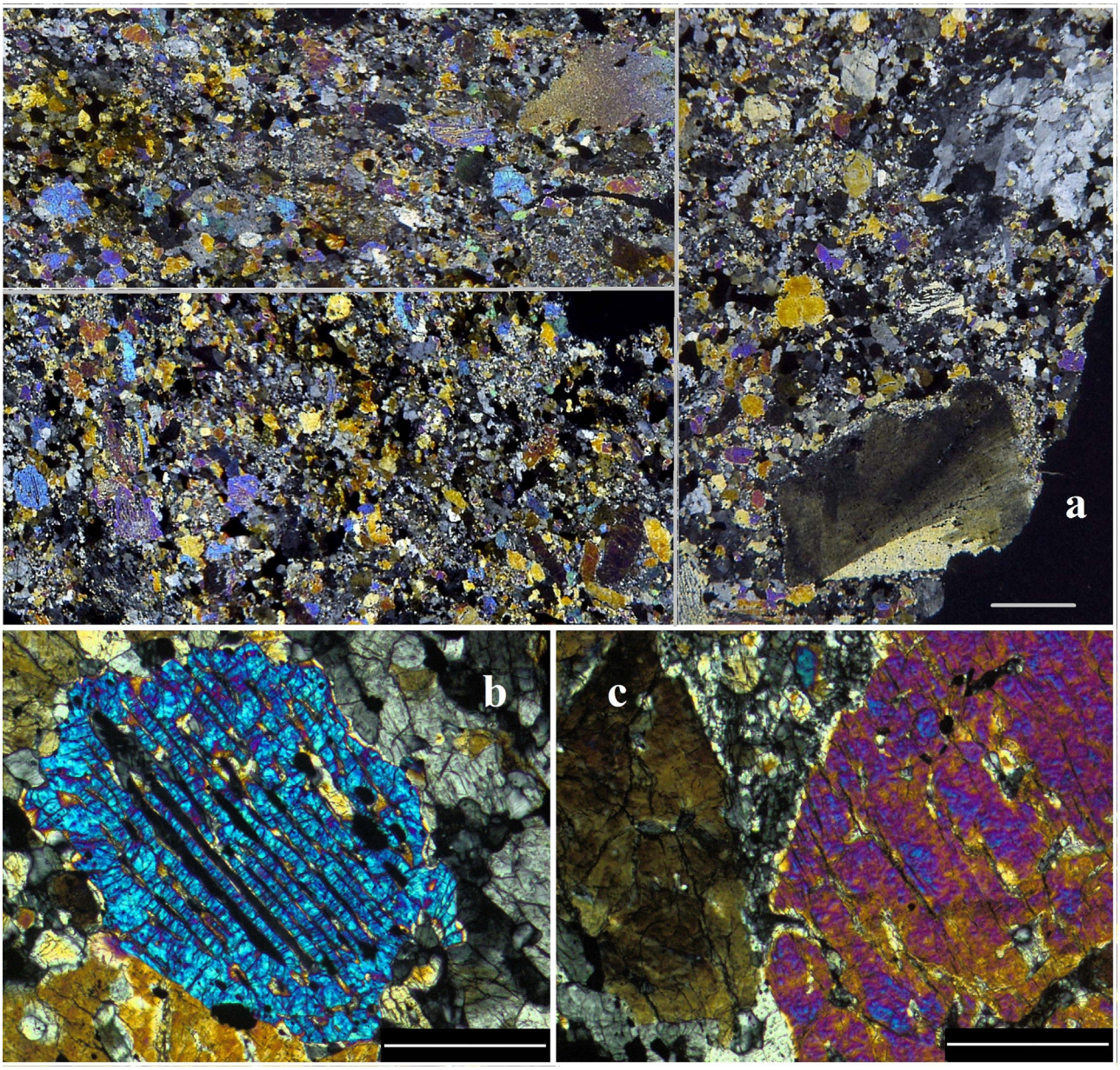

Fig. 5. Thin sections under cross polarized light. a) strongly-recrystallized matrix with mineral fragments, and relict chondrules of various sizes. b) barred-olivine chondrule. c) olivine with weak mosaicsm reflecting shock stage.

Only minor parts of the agricultural landscape were searchable, however, and the search activities ended without more finds.

3. Analytical procedures – summary

This is a brief summary and further details are given in the "Supplementary materials". Several thin and thick sections and fragments of Braunschweig were studied using optical (BML in Gifhorn and Institut für Planetologie in Münster) and electron microscopy. Chemical data by electron microprobe were obtained at the Institut für Geowissenschaften in Kiel and Institut für Planetologie in Münster (Table 2a) and electron microscopic studies with Transmission Electron Microscopes (TEM) were performed at the Institut für Geowissenschaften in Jena. Element distribution maps were generated by micro-XRF at Bruker Nano GmbH in Berlin. The electron backscattered diffraction (EBSD) investigations was obtained at the Bundesanstalt für Materialforschung und – prüfung, Werkstofftechnik in Berlin. Raman and Mössbauer spectroscopical investigations were carried out at the Mineralogische Staatssammlung München (SNSB).

Regarding physical properties, magnetic susceptibility was measured on 96 fragments in Gifhorn, porosity was calculated on an 84 g fragment and on some small fragments, supported by X-ray tomography at the Aix-Marseille Université CNRS, Aix en Provence, while magnetic hysteresis properties of the Braunschweig meteorite were already presented by Gattacceca et al. (2014) in comparison with 90 other ordinary chondrite falls (Table 3). Temperature calculation of troilite α/β phase transformation, specific heat C_p, thermal diffusivity D, and thermal conductivity K, as well as troilite content of Braunschweig were obtained at the Center of Mathematics and Physics and the Institute of Applied Radiation Chemistry in Lodz. FTIR spectroscopic measurements were undertaken using a Bruker Vertex 70 v and a Bruker A513 reflection stage at the IR/IS laboratory located at the Institut für Planetologie in Münster. Additional instrumental and calculation details are given in the "Supplementary materials".

Table 2a
Average compositions of the major phases in the Braunschweig meteorite. Data in wt%; b.d. = below detection limit.

	olivine		poor Ca pyroxene		diopside		feldspar		chromite	
	mean	SD	mean	SD	mean	SD	mean	SD	mean	SD
n	41		39		6		20		8	
SiO_2	37.95	0.98	55.03	0.84	53.40	1.26	66.06	1.32		
TiO_2	b.d.		0.18	0.05	0.39	0.08			2.72	0.37
Al_2O_3	b.d.		0.16	0.02	0.51	0.01	20.98	0.38	5.89	0.55
Cr_2O_3	b.d.		0.12	0.05	0.91	0.05			56.74	1.01
FeO	22.81	0.57	13.86	0.40	5.15	0.19	0.31	0.14	30.96	0.54
MnO	0.46	0.04	0.49	0.04	0.28	0.04			0.43	0.36
MgO	38.44	0.65	28.63	0.39	16.32	0.17			2.83	0.66
CaO			0.83	0.11	21.60	0.30	2.17	0.05		
Na_2O			0.02	0.02	0.61	0.05	9.76	0.37		
K_2O					0.00	0.00	1.08	0.30		
Total	99.75		99.32		99.17		100.37		99.60	
Fa	24.97	0.32								
range	24.3–25.6									
Fs			21.01	0.41	8.32	0.24				
range			20.75–21.72		8.04–8.69					
En			77.38	0.42	46.98	0.20				
range			75.91–78.32		46.70–47.25					
Wo			1.61	0.22	44.70	0.30				
range			1.03–1.81		44.42–45.19					
An							10.27	0.41		
range							9.54–10.94			
Or							6.11	1.72		
range							3.78–9.58			
CRAL									86.61	2.65
range									84.98–88.31	
FFM									86.24	1.05
range									79.80–88.06	

The bulk chemical composition was analysed by using ICP-AES and ICP-SFMS at the Institut Universitaire Européen de la Mer, Université de Bretagne Occidentale in Plouzané, and instrumental neutron activation analysis (INAA) at the Campus Tecnológico e Nuclear in Lisboa (Table 4). Additional instrumental details and information are given in the "Supplementary materials".

Oxygen isotope analysis was carried out at The Open University in Milton Keynes using. The noble gas analyses were made at the Institut für Geowissenschaften in Heidelberg and are reported in Table 5. Additional instrumental details and data are given in the "Supplementary materials".

For determination of cosmogenic radionuclide concentration, non-destructive high purity germanium (HPGe) gamma spectroscopy in the underground laboratories at the Laboratori Nazionali del Gran Sasso was used, while destructive accelerator mass spectrometry (AMS) was obtained at the Space Sciences Laboratory in Berkeley. Additional instrumental and calculation details are given in the "Supplementary materials". The concentrations are reported in Tables 6–8.

A destructive methanolic solvent extraction of organics matter was performed at the Helmholtz-Zentrum in München. Analytical details and information are given in the "Supplementary materials".

4. Results

4.1. Mineralogy and petrology

A detached piece from a completely fragmented individual stone that originally weighed about 1.3 kg (Fig. 1), the 214 g main mass (Fig. 2a) shows a very fragile interior (Fig. 2b). Fifteen further fragments between 84 g and 10 g and more than 300 fragments and splinters >0.1 g were recovered. About 50 g of smaller splinters and dust were also collected. The meteorite is light gray and covered by ~0.4 mm thick layer of black, dull fusion crust with approximately 50 μm wide contraction cracks. Some fragments show metallic slickensides, others present weak conical slickensides on silicate surface. A few meteorite fragments show thin metal-sulfide veins up to 50 μm (Fig. S4). In thin sections, Braunschweig exhibits a strongly recrystallized matrix bearing only a few poorly-defined, relict barred olivine (BO, Fig. 5b), porphyritic olivine-pyroxene (POP), and radial pyroxene (RP) chondrules from 0.5 up to 15 mm in apparent diameter, chondrule and mineral fragments, and black inclusions up to 1.2 mm in size (Fig. 5a). Many fractures running through the meteorite were confirmed by tomography (see below). Some chondrule-like inclusions are heavily recrystallized. One 1 mm yellow-brown inclusion of waxy gloss (Fig. 8a) and some macro chondrules were discovered (Fig. 6b). Major minerals are pyroxene, olivine, plagioclase, troilite, and metal. Accessory minerals are chromite and merrillite. The compositions of representative mineral phases are given in Table 2a. Hochleitner et al. (2014) identified Cr-bearing troilite by Raman spectrometry, but this could not be confirmed by microprobe. Furthermore, Hochleitner et al. (2014) also identified diamond, graphite, and calcite by Raman and Mössbauer spectroscopy. However, these phases can also be due to terrestrial contamination (by cutting and concrete of the target).

Individual olivine grains can reach a size up to 1 mm and their average composition is $Fa_{24.9}$ (range: 24.3–25.6; n = 41). Some olivine crystals and clusters embed chromite crystals ranging between <10 to 30 μm. The low-Ca pyroxenes have a mean composition of $Fs_{21.1}$ (range: $Fs_{20.4–22.7}Wo_{1.0–2.0}$; n = 39) and some large crystals poikilitically enclose olivine. Ca-pyroxene crystals are typically ~50 μm in size and their mean composition is $En_{47}Wo_{45}$ (n = 6). Plagioclase is very common and occurs as interstitial patches up to 0.2 mm in apparent size. Within melt pockets, it is accompanied by chromite and olivine. Some crystals show twin lamellae. Plagioclase is $An_{10–18}Or_{4–11}$ (average: $An_{11}Or_7$; n = 20). About 7 wt% of the meteorite consist of metal that occurs in irregularly-shaped patches up to 0.3 mm dominantly outside the relict chondrules. Inside BO chondrules, metal often occurs as elongated inclusions, interstitial to olivine. Metal patches <20 μm occur as round inclusions. The dominant kamacite contains 4.7–6.2 wt% Ni and 1.0 wt%

Table 2b
Chemical composition of metals. All data in wt%.

	kamacite (n = 8)				taenite (n = 4)			
	mean	SD	min	max	mean	SD	min	max
Fe	76.70	14.65	93.47	95.70	76.63	7.81	65.33	82.73
Ni	5.77	0.50	4.73	6.24	22.40	8.55	16.37	34.99
Co	1.02	0.04	0.96	1.08	0.64	0.21	0.33	0.77
Total	101.09				99.67			

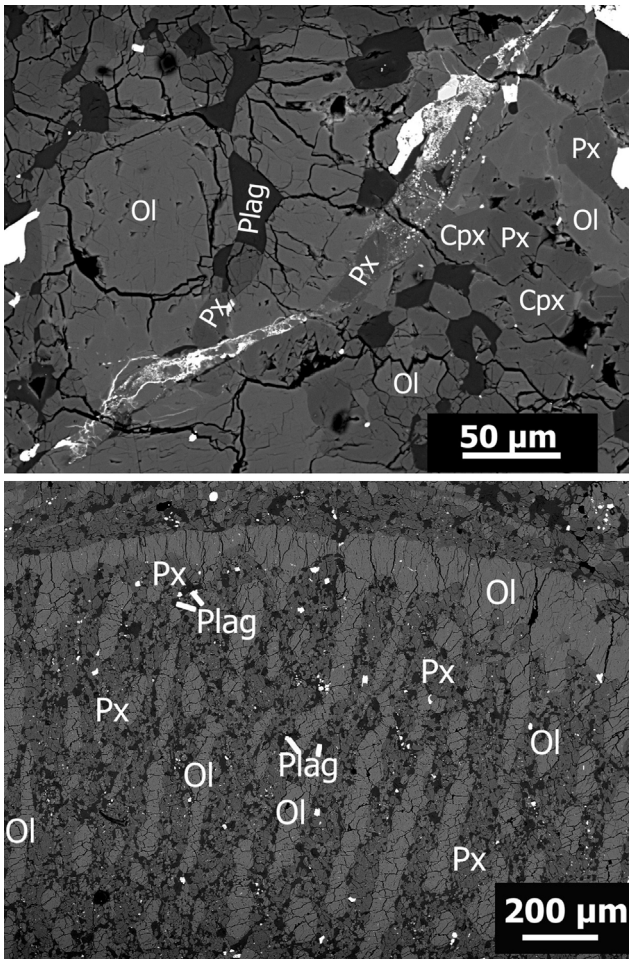

Fig. 6. Back scattered electrons images (Ol – olivine, Px – pyroxene, Cpx – clinopyroxene, Plag – plagioclase): a) Shock vein and internal recrystallized texture. b) heavily fractured barred-olivine macrochondrule.

Table 3
Braunschweig magnetic properties.

log χ	4.22–4.86 × 10^{-9} m^3/kg	this work
B_C	1.70 mT	Gattacceca et al. (2014)
B_{CR}	31.2 mT	Gattacceca et al. (2014)
M_S	17.65 Am^2/kg	Gattacceca et al. (2014)
M_{RS}	7.06 × 10^{-2} Am^2/kg	Gattacceca et al. (2014)
B_C/B_{CR}	18.37	Gattacceca et al. (2014)
M_S/M_{SR}	4.00 × 10^{-3}	Gattacceca et al. (2014)

log χ – magnetic susceptibility, B_C – coercivity, B_{CR} – coercivity of remanence, M_S – saturation magnetization, M_{RS} – saturation remanent magnetization.

Co (n = 8), while taenite has 20–35 wt% Ni and 0.3–0.7 wt% Co (n = 4; Table 2b

). The EBSD images show that the single metal patches are plessitic intergrowths of kamacite and taenite crystallites <20 µm. The crystallites are dominantly elongated, often bent and with low orientation within a single metal grain (Fig. 7a,b). There are kamacite-rich areas with residual taenite grains of 1 µm width, and taenite with perlitic kamacite exsolution (Fig. 11c,d). The Ni concentration in taenite usually reflects the typical M-profile across a lamella, but in some patches this feature is missing. Troilite forms irregularly shaped patches up to 5 mm and dominantly occurs as single brecciated grains, but sometimes with sharp boundaries to metal. Troilite particles smaller than 20 µm appear round. Troilite is also frequently found in the shock veins (Figs. 8 and 10 a) and also in macrochondrules (Hochleitner et al., 2014).

Phosphates and chromites occur as accessory phases. Chromite contains 5.0–6.9 wt% Al_2O_3, 2.1–3.1 wt% TiO_2, and 2.4–4.4 wt% MgO (n = 8). Usually it forms euhedral to subhedral crystals, but within clusters, chromite is coexisting with plagioclase and also shows plate-shaped morphology.

A 1.3 × 1.3 mm-sized Na-Al-Cr-rich inclusion, which is yellow-brown in hand specimen (Fig. 8a), is of "feldspathic" composition. The feldspathic material is embedding chromite crystals of <10 µm and similar in texture and mineralogy to Na-Al-Cr-rich chondrules described earlier (Bischoff and Keil, 1983, 1984). The chromites appear opaque in transmitted plane polarized light. The chromite-free rim of ~50 µm is of Na-Al-rich composition (Na_2O 5.5 ± 1.7, CaO 3.6 ± 1.4, K_2O 1.6 ± 0.2, Al_2O_3 22.4 ± 1.0, SiO_2 67.5 ± 4.5 wt%). FeO and MgO in the silicate phase are <0.6 and<0.03 wt%, respectively. Kamacite (~6.4 wt% Ni, ~0.63 wt% Co) and troilite occur as single grains in the outer rim. The sizes of the euhedral cubic and lath-shaped chromite crystals decrease from 5 to 10 µm in the outer ~20 µm of the inclusion to tiny <1 µm grains in the core (Fig. 8b,c). Mössbauer spectra support the occurrence of Cr-spinel. Al_2O_3 and CaO contents of this inclusion increase from rim to core, whereas SiO_2 and Na_2O decrease. Thus, it appears that the matrix of the inclusion consists of plagioclase being oligoclase at the outer rim and andesite (up to ~An_{50}) in the interior. A very similar inclusion has been found in the Villalbeto de la Pena L6 chondrite (Bischoff et al., 2013).

4.2. Shock effects

Typical olivine shows planar as well as irregular fractures, and weak mosaicism. Ca-poor pyroxene is also heavily fractured and also shows undulate extinction and irregular to planar cracks. Some of the plagioclase grains, which typically show planar deformation features, appear to be partly isotropic. Some shock veins are visible in hand specimen (Fig. 8) as well as in thin section (Fig. 5c). The EBDS maps indicate recrystallized troilite.

TEM observations on olivine (Fig. 9a) using weak-beam dark-field imaging with a diffraction vector **g** = 004 show an abundance of straight dislocations with Burgers vector B = [001] and an orientation of the dislocation line parallel to [001]. These dominantly screw-type dislocations are exclusively unbound (i.e., not aggregated into sub-grain boundaries). The dislocation density observed is approximately 1 × 10^{14} m^{-2}. Enstatite (Fig. 9b) contains thin, 1.8 nm wide, lamellae of clinoenstatite oriented parallel to (100). These lamellae have a width of two clinoenstatite unit cells and share their (100) lattice plane with the host (ortho-)enstatite. The

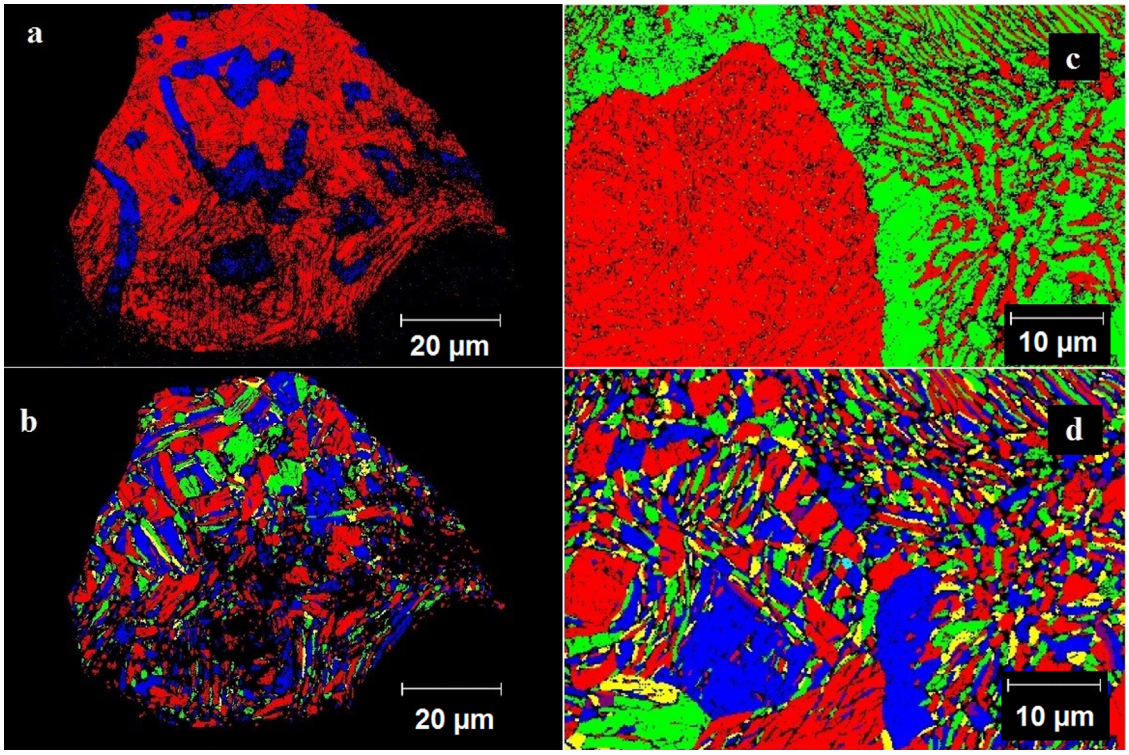

Fig. 7. EBSD show that the single metal patches consist of kamacite and taenite crystallites below 20 µm are in plessitic intergrowth. The crystallites are dominantly elongated, often bent and with low orientation within a single metal grain: a) phase map, red kamacite, blue taenite. b) grain distribution in the same area as a. There are kamacite areas with relict taenite grains of 1 µm and taenite with perlitic kamacite exsolution. c) phase map, red kamacite, green taenite. d) grain distribution in the same area as c. (For interpretation of the references to colour in this figure legend, the reader is referred to the web version of this article.)

spacings observed between the individual clinoenstatite lamellae range between 10 and 100 nm.

4.3. Density

The specific density (bulk density) of Braunschweig meteorite fragments range from 2.9 to 3.2 g/cm^3 in relation to their variable porosities 11–19 vol%. Mean grain density is 3.553 g/cm^3, and, thus, very close to the mean value (3.56 g/cm^3) of L chondrites falls (Consolmagno et al., 2008; Macke, 2010). X-ray tomography shows many open irregular cracks of <5 µm width and up to 50 µm length that cause the high porosity.

4.4. Magnetic susceptibility

Fragments of the meteorite show a wide range of magnetic susceptibilities (log χ = 4.22–4.86; χ in 10^{-9} m^3/kg), with an average of log χ = 4.73 (σ = 0.08. n = 96) based on an average density of 3.1 g/cm^3. According to Consolmagno et al. (2006), the magnetic susceptibility of L chondrite falls are in the range of log χ = 4.76–5.02. Nearly 45% of Braunschweig fragments plot in the L field, whereas 55% reflect the L/LL intermediate group. The lowest log χ of 4·22 was found for a 0.84 g fragment that plots in the LL field and is dominated by a large chondrule fragment.

4.5. Specific heat, thermal diffusivity and thermal conductivity

The specific heat C_p of the meteorite's interior is 530 ± 21 J/(kg K) at −73 °C (200 K), and 727 ± 32 J/(kg K) at 27 °C (300 K). The heat capacity predicted by $C_p(d_{bulk})$ dependence is 737 ± 26 J/(kg K) at 27 °C. The volumetric heat capacity (thermal capacity) is $1.7 \pm 0.2 \times 10^6$ J/(m^3 K) at −73 °C, and $2.3 \pm 0.2 \cdot 10^6$ J/(m^3 K) at RT, which is close to the value characteristic of stony meteorites 2.5×10^6 J/(m^3 K) at room temperature (Szurgot, 2011a). The thermal diffusivity D is $1.0 \pm 0.7 \times 10^{-6}$ m^2/s at −73 °C, and $0.8 \pm 0.5 \times 10^{-6}$ m^2/s at 27 °C, and the thermal conductivity K is 3.7 ± 0.6 W/(m K) at −73 °C, and 3.0 ± 1.6 W/(m K) at 27 °C (Table 9).

The thermal diffusivity and thermal conductivity of Braunschweig vary insignificantly within the temperature range 200–300 K, and the specific heat correlates exponentially with the temperature. Fig. 14 shows the $C_p(T)$ dependence for material representing the interior of the meteorite, and Table 10 presents data for the interior and the edge-crust regions. The mean specific heat capacity of Braunschweig interior increases from 582 to 1132 J/(kgthe thermal conductivityK) within the temperature range of 223–823 K. An extrapolation of the experimental data allows estimation of C_p values at 100, 200, and 990 K (Fig. 10, Table 10). The exponential fit predicts C_p values: 249 ± 10 J/(kgthe thermal conductivityK) at 100 K, and 1165 ± 14 J/(kgthe thermal conductivityK) at 990 K. The heat capacity of material representing edge-crust region exhibits about 20 J/(kg the thermal conductivity K) higher values of C_p than the meteorite interior, due to differences in mineral composition and content (lower troilite and metal content within the crust region) that caused by thermal heating during atmospheric passage. The ratio of two C_p values: 402 J/(kgthe thermal conductivityK) at 150 K, and 727 J/(kgthe thermal conductivityK) at 300 K is equal to 0.55, which is expected since the specific heat capacity of meteorites at temperatures of the asteroid belt objects is established to be about half that of materials measured at room temperature (Consolmagno et al., 2013a,b; Beech et al., 2009; Opeil et al., 2012; Yomogida and Matsui, 1983).

Table 11 compiles room temperature data on thermal conductivity, thermal diffusivity, and specific heat of ordinary chondrites. A comparison of Braunschweig data with literature data (Osako 1981; Yomogida and Matsui, 1983; Beech et al., 2009; Szurgot, 2011b; Szurgot and Wojtatowicz, 2011; Szurgot et al., 2012, 2014b;

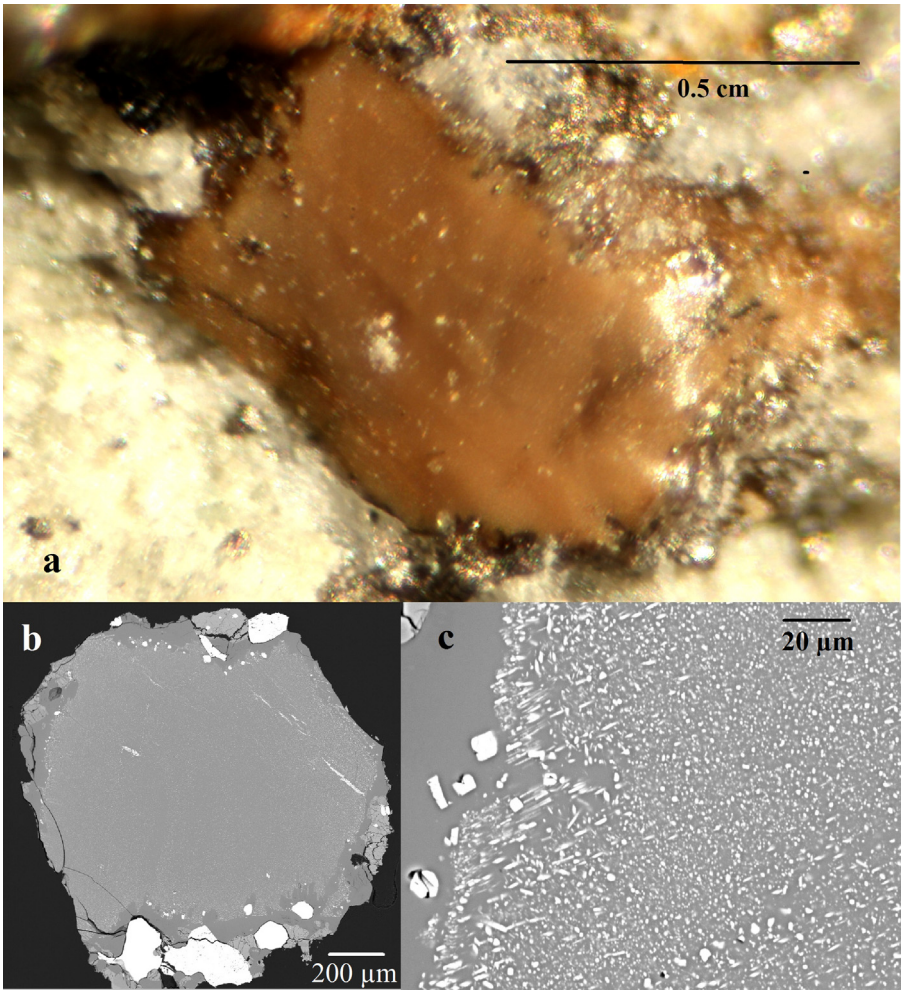

Fig. 8. Na-Al-Cr-rich inclusion: a) in hand specimen, surrounded by metal and troilit; b) SEM shows zoning of Na-Al-Cr-rich inclusion of Fig. 8a. c) detail of Fig. 8b shows gray Cr-free Na-Al-rich feldspathic composition in the rim area and fine Cr-spinel exsolution/white.

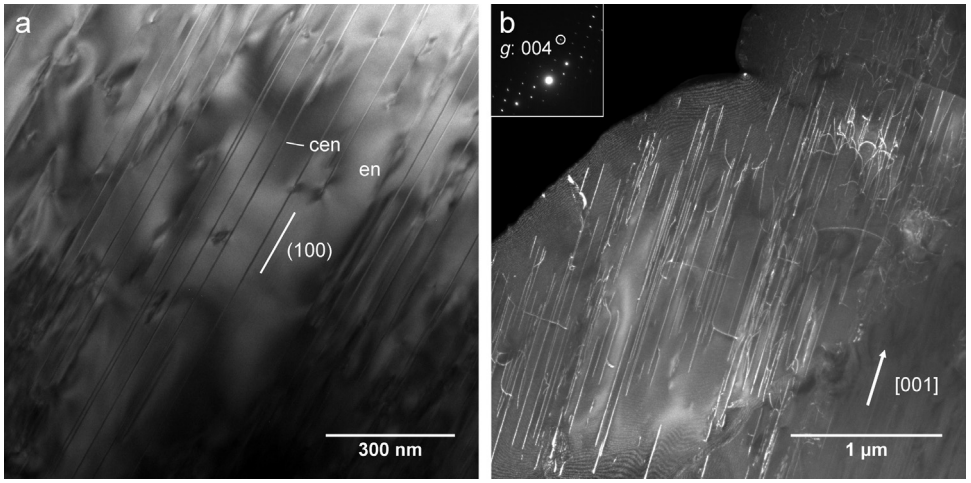

Fig. 9. TEM observations of Braunschweig: a) TEM weak-beam dark-field image of dislocations with **B** = [001] and dominantly screw character in olivine. b) TEM bright-field image of clinoenstatite (cen) lamellae in enstatite (en).

Table 4
Chemical composition of Braunschweig meteorite.

a. ICP.

element	unit	method	bulk
Ti	µg/g	ICP-SFMS	644
Al	wt%	ICP-AES	1.159
Fe	wt%	ICP-AES	21.6
Mn	wt%	ICP-SFMS	0.267
Mg	wt%	ICP-AES	15.0
Ca	wt%	ICP-AES	1.41
Na	wt%	ICP-AES	0.712
K	µg/g	ICP-SFMS	1021
P	wt%	ICP-AES	0.131
Sc	µg/g	ICP-SFMS	10.01
Cr	µg/g	ICP-AES	3804
Co	µg/g	ICP-AES	601
Ni	wt%	ICP-AES	1.23
Be	µg/g	ICP-SFMS	0.0289
V	µg/g	ICP-SFMS	70.09
Cu	µg/g	ICP-SFMS	69.21
Zn	µg/g	ICP-SFMS	43.96
Ga	µg/g	ICP-SFMS	5.05
Rb	µg/g	ICP-SFMS	3.06
Sr	µg/g	ICP-SFMS	11.34
Y	µg/g	ICP-SFMS	2.32
Zr	µg/g	ICP-SFMS	6.48
Nb	µg/g	ICP-SFMS	0.46
Cs	µg/g	ICP-SFMS	0.048
Ba	µg/g	ICP-SFMS	3.78
La	µg/g	ICP-SFMS	0.328
Ce	µg/g	ICP-SFMS	0.873
Pr	µg/g	ICP-SFMS	0.128
Nd	µg/g	ICP-SFMS	0.649
Sm	µg/g	ICP-SFMS	0.218
Eu	µg/g	ICP-SFMS	0.0827
Gd	µg/g	ICP-SFMS	0.3
Tb	µg/g	ICP-SFMS	0.0549
Dy	µg/g	ICP-SFMS	0.378
Ho	µg/g	ICP-SFMS	0.0835
Er	µg/g	ICP-SFMS	0.25
Yb	µg/g	ICP-SFMS	0.256
Lu	µg/g	ICP-SFMS	0.0392
Hf	µg/g	ICP-SFMS	0.197
Ta	µg/g	ICP-SFMS	0.0227
W	µg/g	ICP-SFMS	0.13
Pb	µg/g	ICP-SFMS	0.0336
Th	µg/g	ICP-SFMS	0.0452
U	µg/g	ICP-SFMS	0.0128

b. INAA

element	unit	bulk (a)	bulk (b)
Fe	wt%	23.3	23.4
Mn	wt%	0.236	0.254
Na	wt%	0.738	0.726
K	µg/g	999	963
Sc	µg/g	8.08	8.35
Cr	µg/g	3640	3310
Co	µg/g	719	680
Ni	µg/g	1.27	1.26
Zn	µg/g	54.3	51.1
Ga	µg/g	6.79	6.61
As	µg/g	2.17	1.92
Rb	µg/g	3.08	2.31
Sb	µg/g	n.a.	0.058
La	µg/g	0.125	0.144
Sm	µg/g	0.0504	0.0645
Eu	µg/g	0.0450	0.0440
Tb	µg/g	n.a.	0.058
Ir	µg/g	0.573	0.536
Pt	µg/g	1.08	1.14
Au	µg/g	0.210	0.207
Th	µg/g	0.0441	0.0354

n.a. – not analyzed.

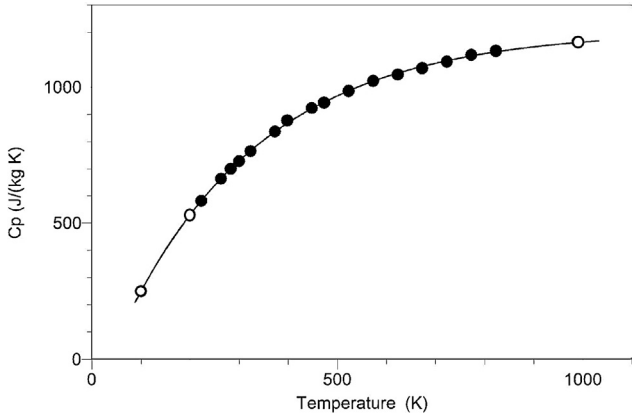

Fig. 10. Specific heat of Braunschweig meteorite as a function of temperature. The fit is given by equation: Cp = A·exp/-C·T +B, where values of coeficients A, B, and C are as follows: A = −1354 ± 6, C = 0.00347 ± 0.00004, B = 1206 ± 4, and RMSE = 4.

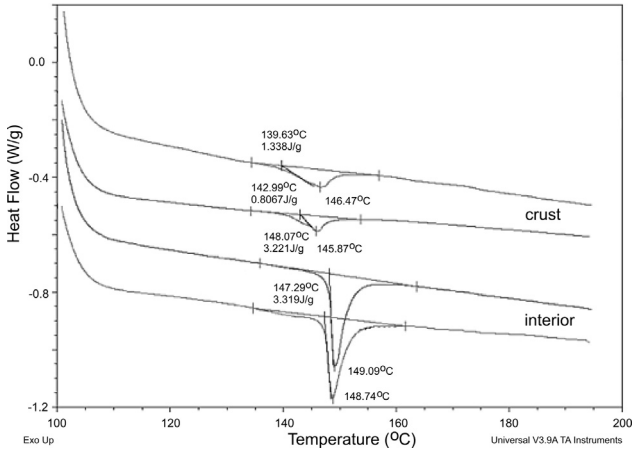

Fig. 11. Heat flow changes during heating of Braunschweig troilite specimens coming from interior and crust regions of the meteorite. Endothermic peaks indicate α/β phase transition of troilite. Onset temperature is regarded as a temperature of the phase transition, and the enthalpy changes are represented as the area under the peaks. Notice: differences between α/β transition temperature, and heat of transition of Baunschweig troilite from interior and crust of meteorite.

Opeil et al., 2010, 2012; Łuszczek and Wach, 2014) indicates that the thermal properties of the Braunschweig L6 chondrite are comparable with the properties of other ordinary chondrites, in particular with properties of L and H chondrites.

4.6. Troilite thermometry: relict temperatures and troilite content

Thermodynamic properties of α/β phase transformations of troilite depend on, and are important indicators of, the thermal history of troilite, and troilite bearing rocks. The maximum temperature achieved during temperature increase during collisions, atmospheric passage, and/or of accretion of this chondrite can be revealed by DSC measurements, and analyzed. Heat flow measurements (DSC) on Braunschweig troilite were performed to decipher shock-related heating temperature, thermal history of the meteorite and its parent body, to determine relict temperatures preserved in troilite located in various regions of the meteorite, and to determine troilite content. Heat flow measurements (DSC) confirmed that the Braunschweig chondrite contains troilite, whose α/β solid-state phase transformations have been detected. Fig. 15 shows heat flow changes during heating of four Braunschweig meteorite specimens as measured by DSC ten months after the fall. Intense, endothermic peaks reveal α/β phase transition of

Table 5
Braunschweig noble gases, cosmic ray exposure and gas retension ages.

	600 °C	1100 °C	1700 °C	total	unit
^{3}He	1024 (7)	8124 (51)	63 (1)	9211 (51)	10^{-11} cm^3 STP/g
^{4}He	b.d.	1944 (23)	48 (19)	2006 (37)	10^{-9} cm^3 STP/g
^{22}Ne	23 (7)	912 (7)	906 (7)	1841 (12)	10^{-11} cm^3 STP/g
^{20}Ne/^{22}Ne	0.775 (220)	0.804 (6)	1.092 (9)	0.945 (10)	
^{21}Ne/^{22}Ne	0.615 (188)	0.792 (6)	0.784 (7)	0.786 (8)	
^{36}Ar	23 (2)	573 (10)	226 (5)	822 (12)	10^{-11} cm^3 STP/g
^{38}Ar/^{36}Ar	0.208 (17)	0.365 (2)	0.633 (5)	0.434 (4)	
^{40}Ar/^{36}Ar	334 (25)	2397 (20)	164 (3)	1725 (19)	
^{84}Kr	259 (22)	220 (46)	192 (27)	672 (58)	10^{-13} cm^3 STP/g
^{83}Kr/^{84}Kr	0.249 (10)	0.256 (13)	0.315 (24)	0.270 (34)	
^{132}Xe	107 (20)	209 (26)	470 (21)	785 (39)	10^{-13} cm^3 STP/g
^{129}Xe/^{132}Xe	0.88 (10)	1.128 (62)	1.255 (35)	1.171 (74)	
^{21}Ne$_c$	0.143 (9)	7.226 (23)	7.094 (27)	14.464 (36)	10^{-9} cm^3 STP/g
^{3}He/^{21}Ne$_c$	71.6 (4.5)	11.24 (8)	0.0891 (16)	6.368 (39)	
(^{22}Ne/^{21}Ne)$_c$	1.637 (54)	1.266 (5)	1.240 (6)	1.256 (4)	
^{38}Ar$_c$	0.005 (4)	1.155 (28)	1.144 (26)	2.304 (42)	10^{-9} cm^3 STP/g
T3 (GCR)	Production rate 1.55·10^{-8} cm^3 STP/(g Ma)	5.9	10^6 a		
T21 (GCR)	Production rate 2.01·10^{-9} cm^3 STP/(g Ma)	7.2	10^6 a		
T38 (GCR)	Production rate 3.12·10^{-10} cm^3 STP/(g Ma)	7.4	10^6 a		
T3 (SCR, 100MeV)	Production rate 2.06·10^{-8} cm^3 STP/(g Ma)	4.5	10^6 a		
T21 (SCR, 100MeV)	Production rate 1.37·10^{-8} cm^3 STP/(g Ma)	1.1	10^6 a		
T38 (SCR, 100MeV)	Production rate 2.00·10^{-9} cm^3 STP/(g Ma)	1.2	10^6 a		
K-Ar age				2.24	10^9 a
U/Th-He age				0.55	10^9 a

Table 6
Massic activities (corrected to the time of fall) of cosmogenic radionuclides (in dpm/kg) in a 26.09 g of the Braunschweig L6 chondrite measured by non-destructive gamma-ray spectrometry. Errors include a 1σ uncertainty of ~10% in the detector efficiency calibration.

Nuclide	Half-life	sample
^{48}V	16.0 d	15 ± 3
^{51}Cr	27.7 d	27 ± 12
^{7}Be	53.1 d	50 ± 9
^{58}Co	70.9 d	3 ± 1
^{56}Co	77.3 d	2 ± 1
^{46}Sc	83.8 d	6 ± 1
^{57}Co	271.8 d	7 ± 1
^{54}Mn	312.3 d	46 ± 5
^{22}Na	2.60 y	69.2 ± 6.4
^{60}Co	5.27 y	<1.1
^{44}Ti	60 y	<3.4
^{26}Al	7.05 × 10^5 y	54.6 ± 4.9

Table 7
Concentrations of cosmogenic radionuclides (in dpm/kg) in a 113.5 mg bulk sample of Braunschweig, measured by accelerator mass spectronomy (AMS) at PRIME Lab.

Nuclide	Half-life (year)	Concentration (dpm/kg)
^{10} Be	1.36 × 10^6	16.3 ± 0.3
^{26}Al	7.05 × 10^5	59.3 ± 0.7
^{36}Cl	3.01 × 10^5	8.0 ± 0.2

troilite. Differences in the α/β transition temperatures T_{on}, T_m, and T_{of} temperatures, and heat of transition (ΔH) of Baunschweig troilite coming from two regions: interior and crust of meteorite can be observed (Fig. 11, Table 12). Temperatures of α/β transitions of troilite reveal temperature gradient existing in the meteorite, and α/β heat transition reveals gradient of troilite content. The interior of the Braunschweig chondrite shows T_{on} = 148.0 ± 0.4 °C, T_m = 149.3 ± 0.3 °C, T_{of} =152.3 ± 0.5 °C, ΔH = 2.0 ± 1.0 J/g, and mean troilite content of 4.8 ± 2.5 wt% (Table 12). Since the mean troilite content of 5.8 ± 0.8 wt% is in the L6 chondrite range of 3.9–7.4 wt% (Jarosewich, 1990), troilite abundance in Braunschweig interior is in the range of L6 chondrites.

DSC measurements of Braunschweig edge-crust area indicates a content of 5.8 ± 0.8 wt% and is in the L6 chondrite range of 3.9–7.4 wt% (Jarosewich, 1990). The crust and adjacent

Table 8
Concentration of primordial radionuclides (ng/g for U and Th and in μg/g for K) in the 26.09 g specimen of the Braunschweig L6 chondrite measured by non-destructive gamma-ray spectrometry. Errors include a 1σ uncertainty of ~10% in the detector efficiency calibration.

Nuclide	sample
U	9 ± 1
Th	34 ± 4
K	785 ± 80

region, the distance up to 2 mm behind the crust boundary, exhibit T_{on} = 141.3 ± 2.4 °C, T_m = 146.2 ± 0.4 °C, T_{of} = 149.8 °C, ΔH = 1.1 ± 0.4 J/g, and troilite content of 2.9 ± 1.0 wt.% (Table 12). DSC peaks of edge-crust samples are about two times broader than those from interior samples. The average troilite content is nearly two times larger in the interior of the meteorite than in the edge-crust region, as is the case for the NWA 6255 L5 chondrite (Łuszczek and Wach, 2014).

Various onset temperatures regarded as α/β phase transformation of troilite (FeS I polymorph) have been established for L chondrites. Sołtmany, NWA 6255, EET83213, and PAT91501 reveal T_{on} temperatures between 145.4 and 148.3 °C (Allton et al., 1994; Szurgot et al., 2012; Łuszczek and Wach, 2014), and are close to those of Braunschweig, and terrestrial Del Norte troilite (148 ± 0.7 °C) (Allton et al., 1993; Allton and Gooding, 1993). However, other L chondrites indicate lower temperatures: 140.7–144.0 °C (Lauer and Gooding, 1996).

To determine relict temperatures (T_{relict}) calibration data for Braunschweig troilite were analyzed. Effect of the maximum temperature of heat treatment on the onset, offset, and peak temperatures of Braunschweig troilite for a constant annealing time of 0.1 min has been used (Fig. 12). It is seen that T_{on}, T_m, and T_{of} temperatures characterizing troilite α/β phase transformation decrease, and DSC peaks become broader with increasing annealing temperature (T_{an}).

According to the calibration data presented in Fig. 12, the following relict temperatures expressed by annealing temperatures ($T_{relict} = T_{an}$) for the Braunschweig meteorite were determined. Extrapolation of $T_{on}(T_{an})$, $T_m(T_{an})$, and $T_{of}(T_{an})$ dependences leads to T_{relict} = 133 ± 23 °C for Braunschweig interior, and calibration for Del Norte troilite at Braunschweig interior onset temperature

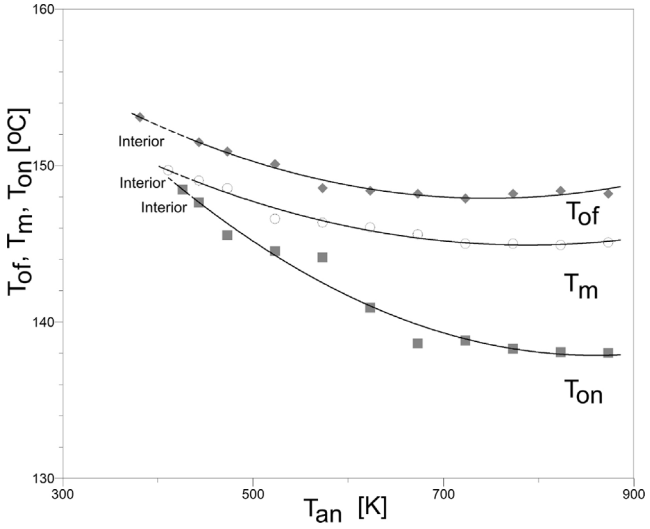

Fig. 12. Effect of maximum temperature of heat treatment T_{an} on onset T_{on}, offset T_{of}, and peak T_m temperatures in Braunschweig troilite. Period of heat treatment at maximum temperature: 0.1 min.

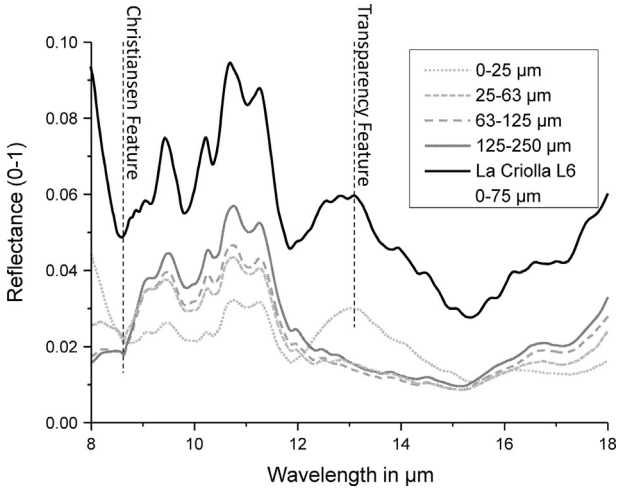

Fig. 13. Braunschweig FTIR spectrum of various grain sizes in comparison to the L 6 chondrite La Criolla/ASTER Spectral Library.

T_{on} = 148.0 °C gives T_{relict} = 135 ± 20 °C (Table 12). Both calibrations give the same relict temperature. Edge-crust regions reveal higher relict temperatures: 246 °C, and 308 °C. $T_{on}(T_{an})$, $T_m(T_{an})$, and $T_{of}(T_{an})$ dependences (Fig. 12) give T_{relict} = 308 ± 46 °C, and Del Norte troilite calibration gives T_{relict} = 246 °C for T_{on} = 141.3 °C (Table 12). These relict temperatures of edge-crust area are reasonable since thermoluminescence data for temperature profiles in ordinary chondrites formed by heating during atmospheric passage give comparable values 239–290 °C for distance 2 mm from the fusion crust boundary (Vaz, 1971, 1972; Sears, 1975; Melcher, 1979).

Relict temperature of Braunschweig interior are noticeable for samples 10–20 mm below the crust. TL data show that during atmospheric passage heating temperatures higher than 120 °C penetrate as far as 20 mm below the surface of the Lost City H5 chondrite, and temperatures above 205 °C penetrate the outer 4 mm of the meteorite (Vaz, 1971). This means that if relict temperatures of the interior is caused by atmospheric heating, the location of Braunschweig interior samples should be 10–15 mm below the fusion crust, but if samples represent the deep interior of the meteorite for depth ≥ 20 mm below the fusion crust, then these relict temperatures indicate a low temperature of accretion of this chondrite (133 °C) or indicate thermal shock during collisions in space or on the parent body.

4.7. Infrared spectroscopy

The FTIR spectrum (Fig. 13) shows the Christiansen Feature (CF), a characteristic reflectance minimum, at 8.6 µm for all size fractions. The finest size fraction (0–25 µm) has the typical Transparency Feature (TF) at 13.1 µm. These features are at band positions typical for pyroxene (Pieters and Englert, 1993). The characteristic Reststrahlen Bands (RB) of the silicates are found at 9.1 µm (shoulder), 9.4–9.5 µm, 10.2–10.3 µm, 10.7–10.8 µm, 11.25 µm, 11.9–12 µm and ~16.8 µm. These bands are typical for forsteritic olivine (9.4–9.5, 10.2–10.3, 10.7–10.8, 11.9 µm and 16.8 µm; Hamilton, 2010), and clino/orthopyroxenes (9.1, 9.4–9.5, 10.2–10.3, 10.7 and 11.25 µm; Hamilton, 2000). Bands of minor mineral phases were not observed.

4.8. Bulk chemical and oxygen isotopic compositions

Chemically Braunschweig is a typical L chondrite as shown by the CI-normalized concentrations (Fig. 14). The REE deviation of the

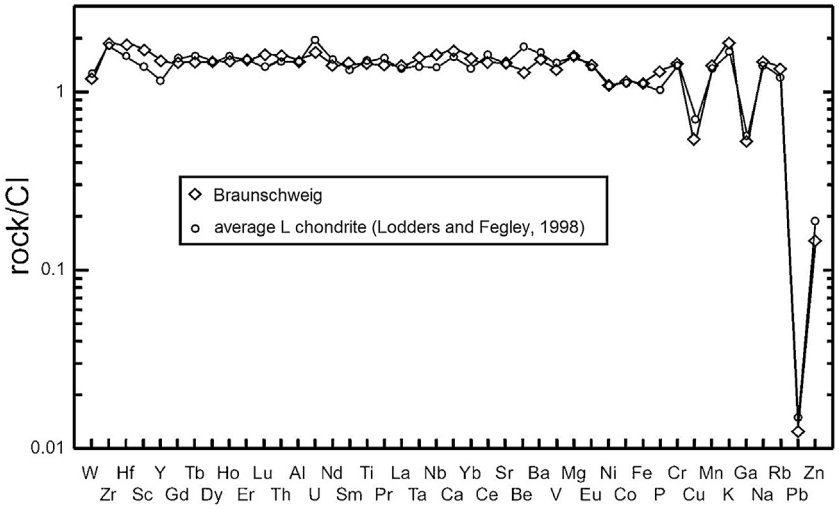

Fig. 14. Braunschweig bulk composition CI-normalized (Barrat et al., 2012, diamonds) reflects typical L chondrite composition (circle, Lodders and Fegley, 1998).

Table 9
Thermophysical properties of Braunschweig L6 chondrite at 200 K and 300 K.

Property [mean/range]	200 K	300 K
Thermal conductivity K [W/(m K)]	3.7 ± 0.6/2.9–4.2	3.0 ± 1.6/1.2–4.1
Thermal diffusivity D [10^{-6} m^2/s]	1.0 ± 0.7/0.45–1.47	0.8 ± 0.5/0.14–1.6
Specific heat capacity C_p [J/(kg K)]	530 ± 21/515–545	727 ± 32/704–749 (737 ± 26[a])
Thermal capacity $C_{volumetric}$ [10^6 J/(m^3 K)]	1.7 ± 0.2	2.3 ± 0.2[b]

[a] Specific heat capacity predicted by C_p (d_{bulk}) dependence.
[b] $C_{volumetric}$ = 2.5·10^6 J/(m^3 K) for stony meteorites (Szurgot, 2011a), and for Sołtmany L6 (Szurgot et al., 2012).

Table 10
Specific heat capacity (J/(kg K) of Braunschweig interior and crust at various temperatures. Extrapolated data are in italic.

T [K]	T [°C]	C_p-interior [mean/range]	C_p-edge-crust [mean/range]	$\Delta\ C_{pcrust}$—$C_{pinterior}$
100	−173	249/249–250	245/241–250	*−4*
200	−73	530/515–545	540/515–565	*10*
223	−50	582/568–596	601/566–637	19
263	−10	663/644–682	684/637–730	21
283	10	699/678–721	720/669–771	21
300	27	727/704–749	748/695–801	21
323	50	764/739–789	786/729–844	22
373	100	836/810–861	864/808–920	28
398	125	877/853–901	916/861–971	39
448	175	922/894–951	942/887–997	20
473	200	942/914–969	962/909–1016	20
523	250	985/962–1007	1002/953–1051	17
573	300	1022/1003–1041	1043/1004–1082	21
623	350	1045/1029–1061	1068/1035k1101	23
673	400	1069/1057–1081	1093/1063–1124	24
723	450	1093/1082–1104	1118/1091–1145	25
773	500	1118/1103–1132	1143/1117–1170	25
823	550	1132/1114–1150	1140/1099–1180	8
990	717	1165/1155–1175	1175/1160–1190	10

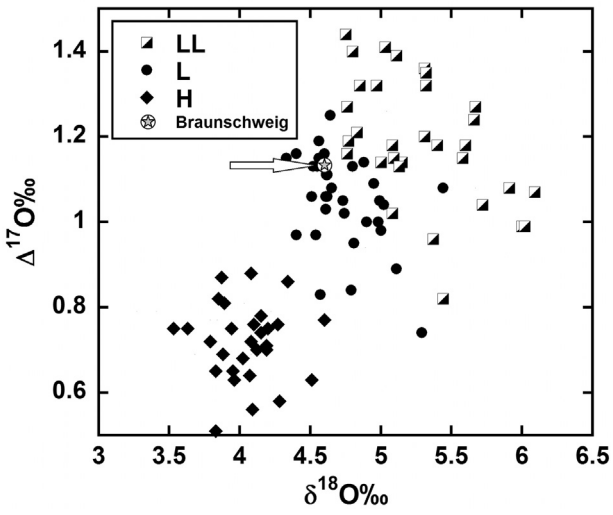

Fig. 15. Oxygen isotope composition of Braunschweig shown in relation to the ordinary chondrite analysis of Clayton et al. (1991).

three analyses are due to inhomogeneous phosphate distribution within the three samples.

Oxygen isotopic analysis of Braunschweig gave the following results: δ^{17}O 3.52‰; δ^{18}O 4.61‰; Δ^{17}O 1.12‰ (Fig. 15), which plot well within the field for L chondrites.

4.9. Radionuclides

Tables 7 and 8 give the measured activities for the short- and medium-lived cosmogenic radionuclides (^{48}V, ^{51}Cr, ^{7}Be, ^{10}Be, ^{58}Co, ^{56}Co, ^{46}Sc, ^{57}Co, ^{54}Mn, ^{22}Na, ^{26}Al) normalized to the date of fall following the simple radioactive decay law. For ^{60}Co and ^{44}Ti, only upper detection limits could be reported. ^{60}Co, ^{54}Mn and ^{22}Na are used to ascertain an approximate depth of the specimen within the meteoroid. The lack of ^{60}Co activity indicate that the specimen either originated from a small meteorite (with radius, R < 20 cm) or was located very close to the surface of a meteoroid with R > 3 cm. The measured sample does not show any evidence of SCR-produced radionuclides; the low ^{51}Cr and ^{56}Co concentrations are consistent with GCR production rates. So the sample was at least a few cm deep. Taken together, the data point to a small radius (<20 cm) body rather than a near-surface location on a larger meteoroid. The data were normalized and compared to the calculations of Eberhardt et al. (1963) and Spergel et al. (1986). The ^{22}Na data were compared to the calculations of Bhandari et al. (1993) for H chondrites, by renormalizing the measured concentration in an L chondrite to that of an H chondrite. If we take the measured activity as saturation value, the likely range of the radius is ≤10 cm. If we assume the sample comes from any part of the meteoroid, it must come from near the surface. The ^{54}Mn were normalised to the concentration of its main target element, Fe. This was compared to the calculations of Kohman and Bender (1967), yielding a radius of ≤5 cm, or a near-surface location on a larger meteoroid. Combining all results of these radionuclides we infer a roughly spherical meteoroid with ≤20 cm radius. This corresponds to a pre-atmospheric mass of less than 114 kg. Adopting the ^{26}Al the production rates in L chondrites from Leya and Masarik (2009), the measured value for ^{26}Al in the 1σ interval of 50 and 60 dpm/kg, indicating a radius of ≤20 cm.

The activities of the short-lived radioisotopes, with half-life less than the orbital period represent the production integrated over the last segment of the orbit. The fall of the Braunschweig L6 chondrite occurred during the current solar cycle 24 maximum, as indicated by the neutron monitor data (Bartol Neutron Monitors, 2013). The cosmic ray flux was relatively low in the six months before the fall. The activities for the very short-lived radionuclides are expected to be low, as earlier reported (Bischoff et al., 2011 and references cited therein).

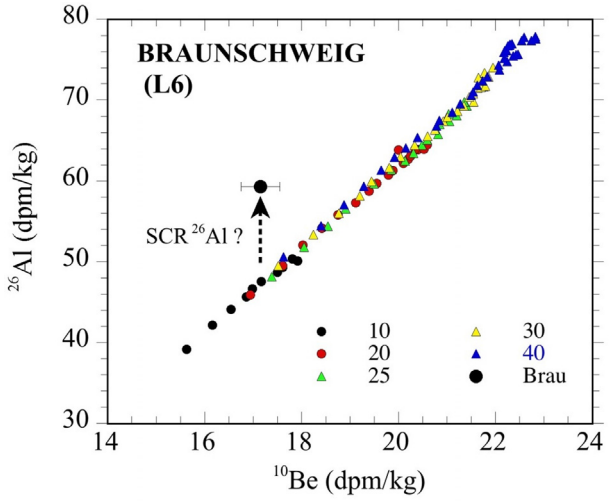

Fig. 16. Production rates of ^{10}Be and ^{26}Al in Braunschweig L6 chondrite relative to calculated production rates for GCR irradiation in L chondrites with radii of 10–40 cm. To derive the ^{10}Be production rate from the measured ^{10}Be concentration, we assumed a CRE age of 6 Ma.

The ^{10}Be activity is 16.3 ± 0.3 dpm/kg, significantly lower than the average L-chondrite production rate of ~20 dpm/kg. This can partly be attributed to undersaturation: the CRE age is ~6 Ma (see below), which corresponds to a ~95% saturation level, yielding a ^{10}Be production rate of 17.2 dpm/kg. The other factor accounting for the low ^{10}Be activity is its exposure in a small pre-atmospheric body. Adopting a ^{10}Be production rate of 17.2 dpm/kg, we infer a pre-atmospheric radius of 10–15, based on the model of Leya and Masarik (2009). The ^{26}Al activity measured by AMS is 59.3 ± 0.7 dpm/kg, slightly higher than the gamma ray result of 54.6 ± 4.9 dpm/kg, but the two measurements are within experimental uncertainties (Table 6). We adopt a weighted average ^{26}Al activity of 59.2 ± 0.7 dpm/kg. This ^{26}Al activity is close to the typical production rate of ~60 dpm/kg in L-chondrites, although it is higher than predicted by the model of Leya and Masarik (2009) given the small pre-atmospheric size we derived based on ^{10}Be (Fig. 16). A possible reconciliation of the ^{10}Be and ^{26}Al data would be that Braunschweig contains a small contribution (~10 dpm/kg) of SCR-produced ^{26}Al, plausible given its small pre-atmospheric size and high ^{22}Ne/^{21}Ne ratio. While the data are suggestive, they are not conclusive. This explanation is not supported by the short-lived radionuclides, which show no evidence of SCR contributions for ^{22}Na, ^{56}Co and ^{51}Cr. The ^{22}Na/^{26}Al ratio of 1.3 ± 0.2 obtained by gamma-ray spectrometry is as it would be expected for its fall date in April 2013, i.e., at the maximum of the relatively weak solar cycle #24. Since the samples measured by gamma-ray spectrometry and AMS/noble gas analysis represent different fragments of the meteorite, it is possible that the 26 g piece used for gamma ray measurements came from a slightly deeper location in the meteoroid than the sample used for AMS and noble gas analyses. Unfortunately, the relative locations of the two samples within the pre-atmospheric object are unknown as the meteorite broke up into small fragments upon impact into the pavement. The unequivocal presence of SCR-produced ^{26}Al can only be demonstrated by measurements from a depth profile from the fusion crust to the interior. Finally, the measured ^{36}Cl concentration of 8.0 ± 0.2 dpm/kg is consistent with the production rate in an object of <20 cm (Leya and Masarik, 2009), although the ^{36}Cl production rate by spallation reactions (on Fe and Ca) is not sensitive to size. The measured ^{36}Cl concentration does indicate a lack of neutron-capture ^{36}Cl, and thus excludes large objects, consistent with the lack of ^{60}Co.

The concentrations of the natural radionuclides ^{232}Th and ^{238}U as well as for K in the meteorite specimens are listed in Table 8. K is well within the average concentration given by Wasson and Kallemeyn (1988) for L chondrites, and with our ICP-AES data. U and Th are 30% and 20% lower, respectively, than the values from Wasson and Kallemeyn (1988) and also below our ICP-AES measurements.

4.10. Noble gas compositions and ^{3}He, ^{21}Ne and ^{38}Ar cosmic-ray exposure ages

Release of noble gases during the heating process differs markedly (Table 5) and likely reflects their distinct host phases and diffusion characteristics. For example, a major release of Ne and Xe was observed at 1700 °C, whereas He and Ar showed their main release at 1100 °C.

Isotope compositions are strongly dominated by contributions of cosmogenic isotopes (^{3}He, ^{21,22}Ne, ^{36,38}Ar, ^{83}Kr) and a minor radiogenic ^{129}Xe excess (^{129}Xe/^{132}Xe = 1.227 ± 0.024 at 1700 °C). The bulk ^{4}He/^{3}He ratio is 21.8 ± 0.4. The ^{40}Ar/^{36}Ar-ratios varied between air-like (at 600 °C), radiogenic (2400 ± 20, at 1100 °C) and a lower than atmospheric composition (164 ± 4, at 1700 °C), mirroring an additional solar-type Ar contribution. Assuming an average K-concentration of 825 ppm (Wasson and Kallemeyn, 1988) and an initial ^{40}Ar/^{36}Ar of zero (=solar), the equivalent total K-Ar age would be 2240 Ma. This indicates a major Ar loss event in the past history of this meteorite, possibly related to its final excavation from its parent body. Preliminary results of a ^{39}Ar-^{40}Ar study reveal clear evidence for partial loss of ^{40}Ar*. We avoided including part of the fusion crust for Ar-Ar dating, but the sample originates from a position close to the meteorites' surface, so it is possible that thermally-induced loss of Ar was related to the atmospheric transit. The highest measured Ar-Ar age of 2578 ± 8 Ma represents a lower limit only of the true Ar-Ar age of Braunschweig. The equivalent total K-Ar age is 2100 Ma, which compares well with our model age derived from noble gas measurements. Similarly, with U and Th concentrations of 12.8 and 45.2 ppb respectively (Table 3), and assuming all ^{4}He stems from the U-Th decay, we obtain a U-Th-He age of ca. 550 Ma. This age is close to the well-documented break-up event of the L-chondrite parent body 470 Ma ago (Korochantseva et al., 2007) and could point to a disturbance of the U-Th-He system leading to loss of ^{4}He* at that time without notably influencing the K-Ar system. Alternatively, He-loss may have occurred recently. In this case the similarity of the calculated U-Th-He age with the 470 Ma break-up age would be coincidental.

The cosmogenic ^{22}Ne/^{21}Ne$_C$ ratio is 1.256 ± 0.004, which is at the upper end of observed values of ordinary chondrites. The ^{22}Ne/^{21}Ne$_C$ ratio is commonly regarded as a shielding parameter indicative of the position of the meteorite within its host meteoroid as well as the (pre-atmospheric) size of the host meteoroid. The rather high value is suggestive of a very small meteoroid size (<20 cm radius). In addition, it may also imply a partial contribution of Ne isotopes produced by solar cosmic-ray (SCR) irradiation and, because of the low penetration depths of solar cosmic rays, a position of our analyzed specimen very close to the pre-atmospheric surface. One possibility to retain this SCR irradiation component within the analyzed specimen is a rather constant orientation of the meteorite during its atmospheric transit, since otherwise ablation of the surface layers would erase the isotopic characteristics of SCR irradiation. Another consequence of the close proximity to the meteoroid surface could be a partial loss of noble gases during atmospheric transit, in particular of ^{3}He. The presence of both SCR and galactic cosmic-ray (GCR) irradiation also influences the calculation of cosmic-ray exposure (CRE) ages, because the production rates of cosmogenic isotopes differ for SCR and GCR, depending

Table 11
Thermophysical properties of H, L, and LL chondrites at 300 K.

Property	Thermal conductivity	Thermal diffusivity	Specific heat capacity
Chondrite	K [W/(m K)]	D [10^{-6} m^2/s]	C_p [J/(kg K)]
Braunschweig L6	3.0 ± 1.6	0.8 ± 0.5	727 ± 32
Sołtmany L6	4.2 ± 0.4 [S12]	1.6 ± 0.2 [S12]	728 [S12]
Lumpkin L6	1.45 [O10]		
Bruderheim L6	0.98 [YM83]	0.39 [YM83]	
Kunashak L6	1.98 [YM83]	0.76 [YM83]	
NWA 6255 L5			668 [LW14]
Gold Basin L4	3.7 [S11b]	1.32 [SW11]	
NWA 4560 LL3.2	4.1 ± 1.3 [S14]	0.9 ± 0.4 [S14]	682 ± 15 [S14]
Gao-Guenie H5	2.99 [B09]	1.21 [B09]	732 [B09]
El Hammami H5	4.5 [S11b]	1.57 [SW11]	
Cronstad H5	1.9 [O10]		
L chondrites	0.45–3.5 [O12]	0.1k1.1 [YM83]	742 [YM83]
	0.4–2.6 [YM83]	0.55–0.75 [O81]	
LL chondrites		0.6–1.0 [YM83]	
H chondrites	1.4–3.2 [O12]	0.26–1.4 [YM83]	714 [YM83]
	0.6–3.5 [YM83]		
Chondrites	1.5–4.5 [S11b]	0.5–2 [SW11]	

References: [S12] Szurgot et al., 2012; [S14] Szurgot et al., 2014b; [O12] Opeil et al., 2012; [S11b] Szurgot, 2011b; [SW11] Szurgot and Wojtatowicz, 2011, [YM83] Yomogida and Matsui, 1983, [O81] Osako, 1981; [B09] Beech et al., 2009; [LW14] Łuszczek and Wach, 2014; [O10] Opeil et al., 2010.

Table 12
α/β transition temperatures/T_{of}, T_m,T_{on}, heat of transition/$\Delta H_{\alpha/\beta}$, troilite content, and relict temperature T_{relict} of Baunschweig meteorite samples representing interior and edge-crust regions measured by DSC ten months after the fall.

Property Samples [no.]	interior [mean ± SD/range] 7	edge&crust [mean ± SD/range] 2
T_{on} [°C]	148.0 ± 0.4/147.3–148.5	141.3 ± 2.4/139.6–143.0
T_m [°C]	149.3 ± 0.3/148.7–149.7	146.2 ± 0.4/145.9–146.5
T_{of} [°C]	152.3 ± 0.5/151.7–153.1	149.8
T_{of}-T_{on} [°C]	4.3	8.5
T_m-T_{on} [°C]	1.3	4.9
T_{of}-T_m [°C]	3.0	3.6
ΔH [J/g]	2.0 ± 1.0/0.9–3.3	1.1 ± 0.4/0.8–1.3
FeS I [wt.%]	4.8 ± 2.5/2.1–8.0	2.9 ± 1.0/2.2–3.6
T_{relict} [°C]	133 ± 23$^{\#}$/108–153 (135 ± 20$^{\#\#}$)	308 ± 46$^{\#}$/256–341 (246$^{\#\#}$)
T_{relict} [K]	406 ± 23$^{\#}$/381–426 (408 ± 20$^{\#\#}$)	581 ± 46$^{\#}$/529–614 (519$^{\#\#}$)

Determined using: $^{\#}$ T_{of}, T_m, and T_{on} and Braunschweig scalling, $^{\#\#}$ Braunschweig T_{of} and calibration data for Del Norte troilite (Allton and Gooding 1993; Allton et al., 1993).

on the shielding depth and SCR energy. Assuming only a contribution of GCR, an average L-chondrite composition (Wasson and Kallemeyn, 1988), a shielding parameter of 1.256 and production rates given by Eugster (1988) and Schultz et al. (1991) (Table 5), the respective exposure ages for ^{3}He, ^{21}Ne and ^{38}Ar would correspond to 5.9 Ma, 7.2 Ma and 7.4 Ma, respectively. On the other hand, if we use the correlation between the ^{21}Ne production rate and the ^{10}Be and ^{26}Al production rates, from the model of Leya and Masarik (2009), we calculate CRE ages of 6.3 Ma (^{21}Ne/^{10}Be) and 4.7 Ma (^{21}Ne/^{26}Al), respectively. Apparently, the exposure ages which are based on GCR production rates correspond to an overestimated value of the shielding parameter (^{22}Ne/^{21}Ne)$_C$ due to an additional solar cosmic-ray induced contribution of Ne$_C$. To account for this effect, we can make use of the measured (bulk-ratios) of ^{3}He$_C$/^{21}Ne$_C$ of 6.37 ± 0.04 and (^{22}Ne/^{21}Ne)$_C$ of 1.256 ± 0.004 (shielding parameter) and determine the mixing ratio between a SCR and GCR contribution, provided no loss of cosmogenic ^{3}He had occurred. Generally, the (^{3}He/^{21}Ne)$_C$ ratio produced during SCR-irradiation is much lower than in case of GCR derived (^{3}He/^{21}Ne)$_C$ production ratio. It is possible to estimate an average exposure age if we know the initial size of the Braunschweig meteoroid and assuming the depth of burial of our specimen. Taking a pre-atmospheric radius of 10 cm as a lower size limit, this could account for a ca. 15–25% contribution of a solar cosmic-ray produced ^{3}He and ^{21}Ne within an approximated energy range of 100–150 MeV. Assuming an average contribution of 20% from SCR and 80% from GCR irradiation and production ratios for a SCR component at 100 MeV energy (Table 5, calculated after Trappitsch and Leya, 2013; with assumption that ^{3}He and tritium production ratios are identical), the corrected ^{3}He, ^{21}Ne and ^{38}Ar CRE ages are 5.6 Ma, 3.3 Ma and 3.6 Ma, respectively. Apparently, the ^{3}He exposure age is rather insensitive to these changes, whereas the ^{21}Ne and ^{38}Ar ages are much younger than considering cosmogenic Ne and Ar production solely by GCR irradiation. Because of the calculation immanent uncertainties related to the size and depth estimates of the Braunschweig meteorite and a possible additional loss of cosmogenic ^{3}He the low ^{21}Ne and ^{38}Ar CRE age values likely underestimate the CRE age. The ^{3}He CRE age of 5.6 Ma thus must be regarded as a lower limit. Similarly, the ^{21}Ne CRE age of 7.2 Ma derived for production by galactic cosmic rays can be considered as an upper limit for the true exposure age of the Braunschweig meteorite. The cosmic ray exposure age between 4.7 Ma (^{21}Ne/^{26}Al) and 7.4 Ma (^{38}Ar) reflects a rather late release from its parent body among the L-chondrites (Fig. 17).

4.11. Organic matter

The ultrahigh-resolution Fourier transform ion cyclotron resonance mass spectrometry (FTICR MS) analysis resulted in more than 6000 resolved mass peaks in negative electrospray ionisation mode ESI(−) (Fig. 18).These m/z values were converted into ~1500 isotope-confirmed elemental compositions by specific combinations of C, H, N, O, and S atoms, building mainly molecular type series CHO, CHNO, CHOS and CHNOS based on a compositional network computation (Tziotis et al., 2011). The visualization of all elemental compositions can be plotted into van Krevelen diagrams which represent the atomic ratios H/C versus O/C in a color code

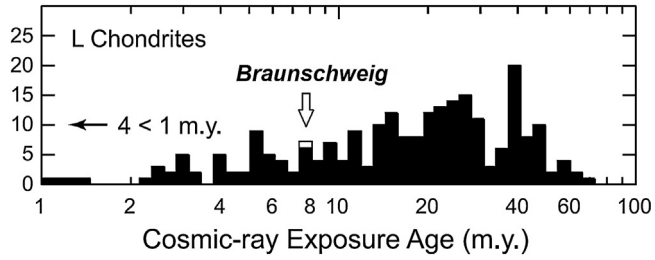

Fig. 17. Cosmic ray exposure age distribution for L chondrites according to Eugster et al. (2006). Braunschweig meteorite reflects a rather late release from its parent body among the L-chondrites.

for the CHO (blue), CHNO (orange), CHOS (green) and CHNOS (red) type of molecules and a bubble size related to the relative intensity of the corresponding ion peaks in the mass spectra (Fig. S5). Braunschweig methanolic extracts showed meaningfully decreases in the number of mass peaks (and of assigned elemental compositions) than the other freshly fallen meteorites of the same petrologic grade like the L6 Soltmany meteorite (Schmitt-Kopplin et al., 2012), Thika (L6, S1, W0) or Battle Mountain (L6, S4, W0), but revealed a typical chondritic signal distribution in the oxidized aliphatic region (Fig. S5).

The classification of the elemental composition based on the distributions of CHO, CHOS, CHNO and CHNOS molecular series showed the relatively high abundance of highly oxygenated aliphatic sulphur containing compounds in ESI(−) FTICR mass spectra (green dots in Fig. S5). The CHOS compounds were almost equally abundant as the CHO compounds with reduced contributions of CHNOS and CHNO molecular series (Fig. S5). Interestingly, the CHNO molecular series with low oxygen contents were found across the entire *m*/*z* range up to the highest molecular masses recorded.

Counting the number of sulphur and nitrogen in all assigned elemental compositions showed that most of the CHOS/CHNOS molecular series contain only single sulphur atom, unlike to nitrogen which showed multiply frequent (up to six folds) in CHNO/CHNOS compositions (Fig. S5). The higher shocked meteorites (Braunschweig and Battle Mountain) showed more oxidized compounds with higher numbers of nitrogen, in agreement with Novato meteorite results (Jenniskens et al., 2014). It should be mentioned that the bimodal distribution of the number of nitrogen in CHNO and of the number of oxygen in CHO molecular series confirms a close link in the chemosynthesis of CHO and CHNO molecular series, as previously modelled (Schmitt-Kopplin et al., 2010).

5. Discussion

5.1. Classification

The L group classification of this equilibrated chondrite is evident from the composition of the major minerals, olivine and pyroxene. The mean composition of olivine (Fa_{25}) and low-Ca pyroxene ($Fs_{21.1}$) are very close to the ranges in $Fa_{22.7–25.6}$, mean $Fa_{24.6}$, and $Fs_{18.7–22.6}$, mean $Fs_{21.3}$ for L group chondrites (e.g., Keil and Fredriksson, 1964; Fodor et al., 1976). In addition, the average plagioclase composition of $An_{11}An_{82}Or_7$ is also very close to the average plagioclase composition for L chondrites of $An_{10.2}Ab_{84.2}$ (Van Schmus and Ribbe, 1968). Finally, a number of physical property measurements confirm the classification of the meteorite as an L group chondrite: The bulk density of Braunschweig, ρ_b, of 3.1 g cm^{-3} is somewhat lower than the 3.40 ± 0.15 g cm^{-3} range for L6 chondrites (Wilkinson and Robinson, 2000) due to a higher porosity. Braunschweig grain density 3.553 g/cm^3 is close to the mean value of 3.56 g/cm^3 of L chondrite falls (Consolmagno et al., 2008; Macke, 2010). Furthermore, the mean value of magnetic susceptibility log χ = 4.73 is similar to that of other L chondrite falls, 4.87 ± 0.10 (Rochette et al., 2003; Consolmagno et al., 2006) and 4.87 ± 0.08 (Smith et al., 2006; Table 13). Furthermore, specific heat, thermal diffusivity, thermal conductivity, troilite α/β transition temperature, enthalpy change, and troilite content also indicate that Braunschweig is an L chondrite.,

The petrologic type 6 of Braunschweig and the shock stage of S4 is evident from microscopic studies of polished thin sections. In detail, only a very small number of chondrule relicts are visible, and plagioclase grains are much larger than 100 μm in apparent size. Thus, Braunschweig is highly recrystallized, and these characteristics clearly indicate that the metamorphosed rock is of petrologic type 6. Typical Braunschweig olivine shows planar fractures and weak mosaicism. These features indicate that the rock is moderately shocked (S4), using the classification scheme of Stöffler et al. (1991).

Mineral microstructures observed by TEM are consistent with a moderate shock stage. In particular, the density of straight screw-type dislocations parallel to the c crystallographic axis is well in agreement with densities observed in other L6 chondrites of shock

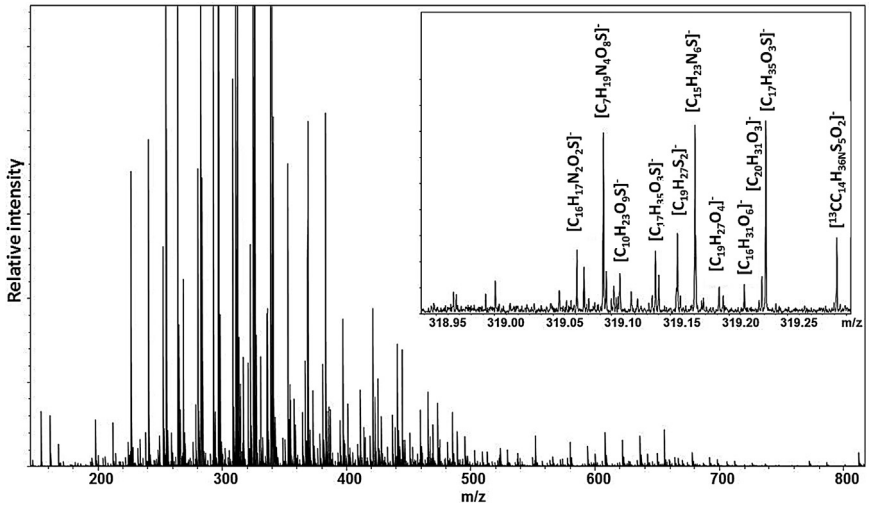

Fig. 18. Mass peaks distribution as detected in ESI(−) FTICR-MS. The excerpt of masses 318.90–319.30 amu/atomic mass unit present the confirmed assigned elemental compositions bearing combinations of C, H, N, O, and S atoms computed based on the NetCalc network software (Tziotis et al., 2011).

Table 13
Braunschweig properties in comparison to ordinary chondrite groups.

	Braunschweig	H	L	LL	Reference
Fa	25.0	16.5–20.8	22.0–26.6	25.8–33.0	Grossman and Rubin (2006)
Fs	21.0	14.5–19.0	19.0–23.0	22.0–27.0	Grossman and Rubin (2006)
An/Ab	10.3/83.6	12.3/81.9	10.2/84.2	10.5/85.9	Van Schmus and Ribbe (1968)
$Co_{kamacite}$ [mg/g]	10.2	4.4–5.1	7.0–9.5	14.2–370	Rubin, (1990)
metal [vol-%]	3.5	8	4	2	Weissberg et al. (2006)
chondrule Ø [mm]	1.5	0.3	0.7	0.9	Weissberg et al. (2006)
Δ17O‰	1.122	0.64–0.82	0.98–1.16	1.14–1.38	Koblitz (2005)
bulk density [g/cm^3]	3.1	2.87–3.74	3.11–3.74	3.10–3.62	Wilkinson and Robinson, (2000)
grain density [g/cm^3]	3.553	3.18–4.14	3.39–3.90	3.41–3.63	Macke (2010)
log χ [x 10^{-9} m^3/kg]	4.73	5.1–5.5	4.7–5.0	3.7–4.7	Consolmagno et al. (2006)

stages S4–S5 (Ruzicka et al., 2015). Their topology and unbound distribution clearly points to an origin by shock deformation and indicates little or absent post-shock annealing (Langenhorst et al., 1995; Ruzicka et al., 2015). Lamellae of clinoenstatite in enstatite are also most likely due to a moderate degree of shock deformation, but other sources of relatively weak shear stress required for their formation cannot be fully excluded (Langenhorst et al., 1995; Jacob et al., 2009).

On most fragments noticeable weathering effects are due to rainy weather and the meteorite discoveries up to five days after the fall. According to Wlotzka (1993), Braunschweig meets the class W0, typical of fresh falls.

Bulk and mineral chemistry, petrology, O-isotopes, and magnetic properties (Gattacceca et al., 2014) are also consistent with the L chondrite group (Keil and Fredriksson, 1964; Wasson and Kallemeyn, 1988; Dunn et al., 2010), while Co in kamacite (0.96–1.08, average 1.02 wt-%, n = 8), magnetic susceptibility (log χ = 4.22–4.86, average 4.73), and visible average chondrule size (1.5 mm) show weak tendencies to the LL group (Consolmagno et al., 2006; Rubin, 1990; Weissberg et al., 2006; Table 13). Large barred-olivine (BO) and radial pyroxene (RP) chondrules did preferentially survive metamorphic recrystallization (Weyrauch and Bischoff, 2012), whereas porphyritic chondrules merge into the bulk rock due to metamorphism and recrystallization.

A comparison with an infrared spectrum of the La Criolla L6 chondrite (Graham, 1985; Baldridge et al., 2009) shows a very good similarity to the Braunschweig size fractions regarding the major bands: a CF at 8.6 μm, a TF at 13.1 μm and TF at 9.1, 9.4, 10.2, 10.7, 11.25 and 16.6 μm. Further minor features occur in the La Criolla sample but not in Braunschweig (e.g., at 8.9, 9.1, 12.6 and 12.8 μm). This could indicate minor differences in mineralogy, but also the loss of features due to impact shock metamorphism (e.g. Johnson, 2012).

5.2. The Braunschweig fall

Despite very limited observational data it turned out that a scenario for the Braunschweig fall with surprisingly well constrained fall parameters could be assembled. The supposed meteoroid fragmentation in 26 ± 2 km height may have produced one or more small meteorites in the range of 10–100 g that were not discovered due to subsequent flooding in the strewnfield.

The originally nose-shaped main mass hit the concrete ground almost vertically after an oriented flight lasting two minutes with a velocity of about 250 km/h. Within less than 1 ms it crushed the concrete pavement to a depth of 3 cm at a pressure of >20 MPa, somewhat below its own compressive strength. Meteorite and concrete powder jets were ejected to form the star-shaped pattern. The deceleration forces exceeded the shear strength in the upper part. Tiny fragments were scattered around at high speed with less than 20% of the mass remaining in the crater. That strong impact did not only break the meteorite into hundreds of fragments and splinters, but also intact fragments show a multitude of internal cracks (Fig. S1), leading to the high porosity in many single specimens, though it had no significant influence on magnetic susceptibility. The wide range of magnetic susceptibility of the single small specimens is dominantly based on the variable particle size of metal and troilite and the distribution of metal poor mega-chondrule fragments. Small chondrules might have vanished during strong recrystallization and incipient shock melting.

Radionuclides present a pre-atmospheric radius of 12–15 cm of the meteoroid and the rather high $^{26}Al/^{10}Be$ ratio for that body size, reflect the presence of SCR-produced ^{26}Al and the minor undersaturation of ^{10}Be due to the short exposure age. The presence of solar cosmic ray influence argues for a stable atmospheric flight that resulted in an oriented meteorite individual with very few ablations on the back-side.

6. Summary

The Braunschweig meteorite fell on April 23rd 2013, with a single totally fragmented stone recovered about 6 h after its fall. The total weight is approximately 1.3 kg. It is an L6 ordinary chondrite with tendencies to LL6, S4-5. Being strongly shocked with gas retention ages of 0.55 Ga (^4He) and 2.24 Ga (^{40}Ar), Braunschweig might have been affected by the catastrophic disruption of the L-chondrite parent body 470 Ma ago (Heck et al., 2004; Schmitz et al., 2009). The bulk composition of the meteorite is very close to the published average element concentration for L-group chondrites. The activities of short-lived cosmogenic radionuclides clearly indicate a very recent meteorite fall. All cosmogenic radionuclide concentrations suggest a rather small pre-atmospheric radius of 12–15 cm for the parent meteoroid, whereas the presence of cosmogenic noble gases indicate a possible SCR influence. The cosmic ray exposure (CRE) ages derived from noble gases are 5.6 Ma (^3He), 7.2 Ma (^{21}Ne) and 7.4 Ma (^{38}Ar), in good agreement with results from radionuclide production (4.7 Ma, $^{21}Ne/^{26}Al$; 6.3 Ma, $^{21}Ne/^{10}Be$), confining the CRE-age to (6.0 ± 1.3) Ma. Due to the oriented atmospheric flight, it is possible that some material from very close to the pre-atmospheric surface has survived atmospheric passage, which may explain the hints of SCR produced cosmogenic nuclides observed in some samples.

The ESI(−) FTICR-MS results revealed that the CHO and CHOS (with single sulphur per molecular formula) elemental compositions of organic compound formulas occluded in Braunschweig are equally and relatively highly abundant when compared to CHNOS and CHNO formulas (with multiply frequent nitrogen) molecular series. Nonetheless a close link in the chemosynthesis of CHO and CHNO compounds, as already observed in many other meteorite types, could be confirmed, based on an original model proposed earlier (Schmitt-Kopplin et al., 2010).

Acknowledgements

We thank Mark Vornhusen (Gais) for the meteor video, Andre Knöfel (Lindenberg) for the light intensity measurement, and the Bundesanstalt für Geowissenschaften und Rohstoffe (Hannover) for access to the seismic database. We also thank the eyewitness Julian Mascow (Wolfenbüttel) for joining us for a detailed interview on site. We gratefully thank Dr. Tomasz Jakubowski and Prof. Tadeusz A. Przylibski, Wrocław University of Technology, for sending us the *Sołtmany* sample for analysis. We thank Mike Farmer and David Cottingham for their donation of the samples of *Thika* and *Battle Mountain,* respectively. This work was partly supported by the German Research Foundation (DFG) within the Priority Program "The First 10 Million Years – a Planetary Materials Approach" (SPP 1385). TEM investigations were supported by Prof. Falko Langenhorst and the DFG (LA 830/14-1). We thank the staff of the RPI of CTN/IST, Portugal for their assistance with the neutron irradiations, and the FCT (Portuguese Science and Technology Foundation) support through the UID/Multi/04349/2013 project. A. Morlok is supported by the DLR funding 50 QW 1302 in the framework of the BepiColombo mission. We also thank Edward Olsen and Klaus Keil for reviewing this manuscript.

Appendix A. Supplementary data

Supplementary data associated with this article can be found, in the online version, at http://dx.doi.org/10.1016/j.chemer.2016.10.004.

References

Łuszczek, K., Wach, R.A., 2014. NWA 6255 meteorite – thermophysical properties of interior and the crust. Meteorites 3, 33–44.
Allton, J.H., Gooding, J.L., 1993. Calorimetric thermometry of meteoritic troilite: a feasibly study. Lunar Planet. Sci. Conf. XXIV, 21–22.
Allton, J.H., Wentworth, S.J., Gooding, J.L., 1993. Calorimetric thermometry of meteoritic troilite: early reconnaissance. Meteoritics 28, 315–316.
Allton, J.H., Wentworth, S.J., Gooding, J.L., 1994. Calorimetric thermometry of meteoritic troilite; preliminary thermometer relationships. Lunar Planet. Sci. Conf. XXV, 25–26.
Baldridge, A.M., Hook, S.J., Grove, C.I., Rivera, G., 2009. The ASTER spectral library version 2.0. Remote Sens. Environ. 113, 711–715.
Barrat, J.A., Zander, B., Moynier, F., Bollinger, C., Liorzou, C., Bayron, G., 2012. Geochemistry of CI chondrites: major and trace elements, and Cu and Zn Isotopes. Geochim. Cosmochim. Acta 83, 79–92.
Bartol Neutron Monitors, 2013. http://neutronm.bartol.udel.edu/.
Beech, M., Coulson, I.M., Wenshuang, N., McCausland, P., 2009. The thermal and physical characteristics of the Gao-Guenie (H5) meteorite. Planet. Space Sci. 57, 764–770.
Bhandari, N., Mathew, K.J., Rao, M.N., Herpers, U., Bremer, K., Vogt, S., Wölfli, W., Hofmann, H.J., Michel, R., Bodemann, R., Lange, H.-J., 1993. Depth and size dependence of cosmogenic nuclide production rates in stony meteoroids. Geochim. Cosmochim. Acta 57, 2361–2375.
Bischoff, A., Keil, K., 1983. Catalog of Al Rich Chondrules, Inclusions and Fragments in Ordinary Chondrites. Special Publication No. 22. UNM, Institute of Meteoritics, Albuquerque, pp. 1–33.
Bischoff, A., Keil, K., 1984. Al-rich objects in ordinary chondrites, related origin of carbonaceous and ordinary chondrites and their constituents. Geochim. Cosmochim. Acta 48, 693–709.
Bischoff, A., Jersek, M., Grau, T., Mirtic, B., Ott, U., Kučera, J., Horstmann, M., Laubenstein, M., Herrmann, S., Randa, Z., Weber, M., Heusser, G., 2011. Jesenice – a new meteorite fall from Slovenia. Meteorit. Planet. Sci. 46, 793–804.
Bischoff, A., Dyl, K.A., Horstmann, M., Ziegler, K., Wimmer, K., Young, E.D., 2013. Reclassification of Villalbeto de la Peña – occurrence of a winonaite-related fragment in a hydrothermally metamorphosed polymict L-chondritic breccia. Meteorit. Planet. Sci. 48, 628–640.
Ceplecha, Z., Borovička, J., Elford, W.G., ReVelle, D.O., Hawkes, R.L., Porubčan, V., Šimek, M., 1998. Meteor phenomena and bodies. Space Sci. Rev. 84, 327–471.
Clayton, R.N., Mayeda, T.K., Goswani, J.N., Olsen, E.J., 1991. Oxygen isotope studies of ordinary chondrites. Geochim. Cosmochim. Acta 55, 2317–2337.
Consolmagno, G.J., Macke, R.J., Rochette, P., Britt, D.T., Gattacceca, J., 2006. Density, magnetic susceptibility, and the characterization of ordinary chondrite falls and showers. Meteorit. Planet. Sci. 41, 331–342.
Consolmagno, G.J., Britt, D.T., Macke, R.J., 2008. The significance of meteorite density and porosity. Chemie der Erde 68, 1–29.
Consolmagno, G.J., Schaefer, M.W., Schaefer, B.E., Britt, D.T., Macke, R.J., Nolan, M.C., Howell, E.S., 2013a. Low temperature heat capacities of solar system materials. European Planet. Sci. Congress 2013, 2013, EPSC Abstracts 8 EPSC 2013–248.
Consolmagno, G.J., Schaefer, M.W., Schaefer, B.E., Britt, D.T., Macke, R.J., Nolan, M.C., Howell, E.S., 2013b. The measurement of meteorite heat capacity at low temperatures using liquid nitrogen vaporization. Planet. Space Sci. 87, 146–156.
Dunn, T.L., Mc Sween, H.Y., McCoy, T.J., Cressey, G., 2010. Analysis of ordinary chondrites using powder X-ray diffraction, 2. Applications to ordinary chondrite parent-body processes. Meteorit. Planet. Sci. 45, 135–156.
Eberhardt, P., Geiss, J., Lutz, H., 1963. Neutrons in meteorites. In: Geiss, J., Goldberg, E.D. (Eds.), Earth Science and Meteoritics. North Holland Publ. Co., Amsterdam, pp. 143–168.
Eugster, O., Herzog, G.F., Marti, K., Caffee, M.W., 2006. Irradiation records, cosmic-Ray exposure ages, and transfer times of meteorites. In: Lauretta, D., McSween, H.Y. (Eds.), Meteorites and the Early Solar System II. Arizona University Press, Tucson, pp. 829–852.
Eugster, O., 1988. Cosmic-ray production rates for ^{3}He, ^{21}Ne, ^{38}Ar, ^{83}Kr, and ^{126}Xe in chondrites based on ^{81}Kr-Kr exposure ages. Geochim. Cosmochim. Acta 52, 1649–1662.
Fodor, R.V., Keil, K., Wilkening, L.L., Bogard, D.D., Gibson, E.K., 1976. Origin and history of a parent body regolith breccia, Carbonaceous and noncarbonaceous lithic fragments in the Abbott, New Mexico, chondrite. In: Tectonics and Mineral Resources of Sotuhwestern North America. New Mexico Geological Society, pp. 206–218 (Special Publication 6).
Gattacceca, J., Suavet, C., Rochette, P., Weiss, B.P., Winklhofer, M., Uehara, M., Friedrich, J.M., 2014. Metal phases in ordinary chondrites, Magnetic hysteresis properties and implications for thermal history. Meteorit. Planet. Sci. 49 (4), 652–676.
Graham, A.L., 1985. Meteoritical bulletin, No. 63. Meteoritics 20, 275–283.
Grossman, J., Rubin, A. White paper report for the Nomenclature Committee on the composition of olivine and pyroxene in equilibrated ordinary chondrites http://www.lpi.usra.edu/meteor/docs/whitepaper.pdf.
Hamilton, V.E., 2000. Thermal infrared emission spectroscopy of the pyroxene mineral series. J. Geophys. Res. 105, 9701–9716.
Hamilton, V.E., 2010. Thermal infrared (vibrational) spectroscopy of Mg-Fe olivines A review and applications to determining the composition of planetary surfaces. Chemie der Erde 70, 7–33.
Heck, P.R., Schmitz, B., Baur, H., Halliday, A.N., Wieler, R., 2004. Fast delivery of meteorites to Earth after a major asteroid collision. Nature 430, 323–325.
Hochleitner, R., Hoffmann, V.-H., Kaliwoda, M., Bartoschewitz, R., 2014. New data on the braunschweig meteorite (L6) – a recent fall in Germany (2013) (abstract OAp02). In: National Institute of Polar Research Meeting, Tokyo.
Jacob, D., Stodolna, J., Leroux, H., Langenhorst, F., Houdellier, F., 2009. Pyroxenes microstructure in comet 81P/Wild 2 terminal stardust particles. Meteorit. Planet. Sci. 44, 1475–1488.
Jarosewich, E., 1990. Chemical analyses of metorites, a compilation of stony and iron metorite analyses. Meteoritics 25, 323–337.
Jenniskens, P., Rubin, A.E., Qin, Q.-Z., Sears, D.W.G., Sandford, S.A., Zolensky, M.E., Krot, A.N., Blair, L., Kane, D., Utas, J., Verish, R., Friedrich, J.M., Wimpenny, J., Eppich, G.R., Ziegler, K., Verosup, K.L., Rowland, D.J., Albers, J., Gural, P.S., Grigsby, B., Fries, M.D., Matson, R., Johnston, M., Silber, E., Brown, P., Yamakawa, A., Sanborn, M.E., Laubenstein, M., Welten, K.C., Nishiizumi, K., Meier, M.M.M., Busemann, H., Clay, P., Caffee, M.W., Schmitt-Kopplin, P., Hertkorn, N., Glavin, D.P., Callahan, M.P., Dworkin, J.P., Wu, Q., Zare, R.N., Grady, M., Verchovsky, S., Emel'Yanenkov, V., Naroenkov, S., Clark, D. l., Girten, B., Worden, P.S., 2014. Fall. Recovery and characterization of the Novato L6 chondrite breccia. Meteorit. Planet. Sci. 49 (8), 1388–1425.
Johnson, J.R., 2012. Thermal infrared spectra of experimentally shocked andesine anorthosite. Icarus 221, 359–364.
Keil, K., Fredriksson, K., 1964. The iron. magnesium. and calcium distribution in coexisting olivines and rhombic pyroxenes of chondrites. J. Geophys. Res. 69, 3487–3515.
Koblitz, J., 2005. MetBase 7.1. © J. Koblitz, Fischerhude, Germany.
Kohman, T.P., Bender, M.L., 1967. Nuclide production by cosmic rays in meteorites and on the Moon. High-Energy Nuclear Reactions in Astrophysics. In, High-Energy Nuclear Reactions in Astrophysics – A Collection of Articles. (Eds.) Shen B.S.P., Benjamin W. A., New York. N.Y. pp. 169–245.
Korochantseva, E.V., Trieloff, M., Lorenz, C.A., Buykin, A.I., Ivanova, M.A., Schwarz, W.H., Hopp, J., Jessberger, E.K., 2007. L-chondrite asteroid breakup tied to Ordovician meteorite shower by multiple isochron ^{40}Ar-^{39}Ar dating. Meteorit. Planet. Sci. 42, 113–130.
Langenhorst, F., Joreau, P., Doukhan, J.C., 1995. Thermal and shock metamorphism of the Tenham chondrite A TEM examination. Geochim. Cosmochim. Acta 59, 1835–1845.
Lauer Jr., H.V., Gooding, J.L., 1996. Troilite cosmothermometer, application to L-chondrites. Lunar Planet. Sci. Conf. XXVII, 731–732.
Leya, I., Masarik, J., 2009. Cosmogenic nuclides in stony meteorites revisited. Meteorit. Planet. Sci. 44, 1061–1086.
Lodders, K., Fegley Jr., B., 1998. The Planetary Scientist's Companion. Oxford University Press, New York (371 pp.).
Macke, R.J., 2010. Survey of Meteorite Physical Properties, Density, Porosity and Magnetic Susceptibility, Ph.D. Thesis. University of Central Florida, Orlando.
Melcher, C.L., 1979. Kirin meteorite temperature gradient produced during atmospheric passage. Meteoritics 14, 309–316.

Opeil, C.P., Consolmagno, G.J., Britt, D.T., 2010. The thermal conductivity of meteorites, new measurements and analysis. Icarus 208, 449–454.
Opeil, C.P., Consolmagno, G.J., Safarik, D.J., Britt, D.T., 2012. Stony meteorites thermal properties and their relationship with meteorite chemical and physical states. Meteorit. Planet. Sci. 47, 319–329.
Osako, M., 1981. Thermal diffusivity measurements of chondrites and iron meteorite. Bull. Natl. Sci. Museum Tokyo, Ser. E 4, 1–8.
Pieters, C.M., Englert, P.A.J., 1993. Remote Geochemical Analysis. Elemental and Mineralogical Composition. Cambridge University Press.
Rochette, P., Sagnotti, L., Bourot-Denise, M., Consolmagno, G., Folco, L., Gattacceca, J., Osete, M.L., Pesonen, L., 2003. Magnetic classification of stony meteorites 1. Ordinary chondrites. Meteorit. Planet. Sci. 38, 251–268.
Rubin, A.E., 1990. Kamacite and olivine in ordinary chondrites, intergroup and intragroup relationships. Geochim. Cosmochim. Acta 54, 1217–1232.
Ruzicka, A., Hugo, R., Hutson, M., 2015. Deformation and thermal histories of ordinary chondrites, evidence for post-deformation annealing and syn-metamorphic shock. Geochim. Cosmochim. Acta 163, 219–233.
Schmitt-Kopplin, P., Gabelica, Z., Gougeon, R.D., Fekete, A., Kanawati, B., Harir, M., Gebefuegi, I., Eckel, G., Hertkorn, N., 2010. High molecular diversity of extraterrestrial organic matter in Murchison meteorite revealed 40 years after its fall. PNAS 107 (7), 2763–2768.
Schmitt-Kopplin, P., Harir, M., Kanawati, B., Tziotis, D., Hertkorn, N., Gabelica, Z., 2012. Chemical footprint of the solvent soluble extraterrestrial organic matter occluded in Sołtmany ordinary chondrite. Meteorit. J. 1–2, 79–92, Special Issue Soltmany.
Schmitz, B., Harper, D.A.T., Peucker-Ehrenbrink, B., Stouge, S., Alwmark, C., Cronholm, A., Bergström, S.M., Tassinari, M., Wang, X., 2009. Asteroid breakup linked to the great ordovician biodiversification event. Nat. Geosci. 1, 49–53.
Schultz, L., Weber, H.W., Begemann, F., 1991. Noble gases in H-chondrites and potential differences between Antarctic and non-Antarctic meteorites. Geochim. Cosmochim. Acta 55, 59–66.
Sears, D.W., 1975. Temperature gradients in meteorites produced by heating during atmospheric passage. Mod. Geol. 5, 155–164.
Smith, D.L., Ernst, R.E., Samson, C., Herd, R., 2006. Stony meteorite characterization by non-destructive measurement of magnetic properties. Meteorit. Planet. Sci. 41, 355–373.
Spergel M.S., Reedy R.C., Lazareth O.W., Levy P.W., Slatest L.A., 1986. Cosmogenic neutron-capture-produced nucleides in stony meteorites. 16th Proceedings of the Lunar & Planetary Science Conference, J. Geophys. Res., Suppl. (91), D483–D494.
Stöffler, D., Keil, K., Scott, E.R.D., 1991. Shock metamorphism of ordinary chondrites. Geochim. Cosmochim. Acta 55, 3845–3867.
Szurgot, M., Wojtatowicz, T.W., 2011. Thermal diffusivity of meteorites. Meteorit. Planet. Sci. 46 (S1 Suppl. (1)), A230.
Szurgot, M., Wach, R.A., Przylibski, T.A., 2012. Thermophysical properties of the Soltmany meteorite. Meteorites 2, 53–65.
Szurgot, M., Wach, R.A., Matusiak, M., 2014b. Thermophysical properties of NWA 4560. chondrite. Meteorit. Planet. Sci. 49 (S1 Suppl. (1)), A388.
Szurgot, M., 2011a. On the specific heat capacity and thermal capacity of meteorites. Lunar Planet. Sci. Conf. XXXXII (#1150).
Szurgot, M., 2011b. Thermal conductivity of meteorites. Meteorit. Planet. Sci. 46 (S1 Suppl. (1)), A230.
Trappitsch, R., Leya, I., 2013. Cosmogenic production rates and recoil loss effects in micrometeorites and interplanetary dust particles. Meteorit. Planet. Sci. 48, 195–210.
Tziotis, D., Hertkorn, N., Schmitt-Kopplin, P., 2011. Kendrick-analogous network visualisation of ion cyclotron resonance fourier transform (FTICR) mass spectra, improved options to assign elemental compositions and to classify organic molecular complexity. Eur. J. Mass Spectrom. 17, 415–421.
Van Schmus, W.R., Ribbe, P.H., 1968. The composition and structural state of feldspar from chondritic metreorites. Geochim. Cosmochim. Acta 32, 1327–1342.
Vaz, J.E., 1971. Lost city meteorite, determination of the temperature grandient induced by atmospheric friction using thermoluminescence. Meteoritics 6 (3), 207–216.
Vaz, J.E., 1972. Ucera meteorite, determination of differential atmospheric heating using its natural thermoluminescence. Meteoritics 7 (2), 77–86.
Wasson, J.T., Kallemeyn, G.W., 1988. Compositions of chondrites. Philos. Trans. R. Soc. Lond. Ser. A Math. Phys. Sci. 325 (1587), 535–544 (The Solar System, Chemistry as a Key to Its Origin).
Weissberg, M.K., McCoy, T.J., Krot, A.N., 2006. Systematics and evaluation of meteorite classification. In: Lauretta, D., McSween, H.Y. (Eds.), Meteorites and the Early Solar System II. Arizona University Press, Tucson, pp. 19–52.
Weyrauch, M., Bischoff, A., 2012. Macro chondrules in chondrites – Formation by melting of mega-sized dust aggregates and/or by rapid collisions at high temperatures? Meteorit. Planet. Sci. 47, 2237–2250.
Wilkinson, S.L., Robinson, M.S., 2000. Bulk density of ordinary chondrite meteorites and implications for asteroidal internal structure. Meteorit. Planet. Sci. 35, 1203–1213.
Wlotzka, F., 1993. A weathering scale for the ordinary chondrites. Meteoritics 28, 460.
Yomogida, K., Matsui, T., 1983. Physical properties of ordinary chondrites. J. Geophys. Res. 88, 9513–9533.